Mechanics of Materials 140 (2020) 103220

Contents lists available at ScienceDirect

Mechanics of Materials

journal homepage: www.elsevier.com/locate/mechmat

Research paper

Dynamic compression behaviors of concrete under true triaxial confinement: An experimental technique

Songlin Xu[a], Junfang Shan[a,*], Lei Zhang[a], Lijiang Zhou[a], Guangfa Gao[b], Shisheng Hu[a], Pengfei Wang[a,*]

[a] CAS key Laboratory for Mechanical Behavior and Design of Materials, Department of Modern mechanics, University of Science and Technology of China, Hefei, Anhui 230027, China
[b] School of Mechanical Engineering, Nanjing University of Science and Technology, Nanjing, Jiangsu 210094, China

ARTICLE INFO

Keywords:
Impact dynamics
Static triaxial confinement
Concrete
Loading path effect
Strain rate effect
The Drucker-Prager (D-P) criterion

ABSTRACT

A dynamic testing system for concrete-like material under static triaxial confinements is developed in the present article. The cubic specimen with length 50 mm is constrained by six steel square bars. The static triaxial confinements are applied on the specimen through six steel bars that independently servo-controlled by three hydraulic cylinders. A striker is then launched to impact the incident bar along the x-axis. The dynamic responses of the cubic specimen are measured by strain gauges stuck on the middle surfaces of the six bars. The dynamic compressive behaviors of concrete specimens under various static triaxial confinements are investigated accordingly. The 3-D dynamic engineering stress- engineering strain relationship, the dynamic volumetric strain-hydrostatic pressure relationship, and the equivalent stress- equivalent strain relationship are obtained and analyzed in details. The results show evidently the load path dependence and the strain rate dependence. Based on the Drucker-Prager (D-P) strength criterion, the effect of the intermediate stress on dynamic strength is discussed, and the material parameters (e.g. α_0 and k_0) and the strength parameters (e.g. the cohesion c and the inner friction angle ϕ) at various strain rates are demonstrated. The results show that with increasing strain rate, the friction angle ϕ increases, and the cohesion c decreases. The technique provides profound and comprehensive understanding of the dynamic failure properties for concrete-like material under complex stress states.

1. Introduction

Dynamic behaviors of concrete-like material (e.g. concrete, mortar, rock) subjected to impact loading had attracted great concerns in the designing and construction of a variety of concrete structures (e.g. dam, high-rise building, airport runway) in the fields of geotechnical engineering, mining engineering, hydraulic engineering, and defense engineering, etc. Since concrete-like materials are composed of cement, sand, coarse aggregates, etc., they are artificially complex medium and take on load-path dependence, geometry dependence, and strain-rate dependence. Many numerical and experimental results had showed that although under uniaxial compression, dynamic strengths of the concrete-like materials were sensitive to the hydrostatic stress due to the local lateral inertia confinement (Burlion et al., 2000; Grote et al., 2001; Li and Meng, 2003; Meng and Li, 2003a,b; Tang et al., 2005), which might cause obvious increase of the dynamic increase factor (DIF) between the nominal strain-rate 10^2 and 10^3 s^{-1} (Ross et al., 1989; 1995; 1996; Zhang and Zhao, 2014). The accurate material characterization taking into account the stress triaxiality and strain rate effect are required in engineering designs of concrete structures under complicated loading conditions. This article would propose a new experimental apparatus to investigate both the load-path dependent and the strain-rate dependent properties of concrete specimens under true triaxial confinement.

Many significant conclusions had been obtained for concrete and rock-like materials under quasi-static triaxial confinement (Handin et al., 1967; Mogi, 1967, 1971; Gerstle, 1980; Horii and Nemat-Nasser, 1986; Lubarda et al., 1996). Under lower confinement, failure patterns of specimen turned with increasing confinements, i.e. from the axial splitting pattern, the faulting pattern, to the narrow shear band with high concentration interacting microcracks. Under higher confinements, the failure of specimens were caused by the distributed grain-scale crushing and the homogenous microcracking, and the failure pattern showed plastic flowing properties at the macro scale. Volume decreases in the process were normally higher than 10 percent, and some complex mechanisms were introduced, e.g. ductile fracture,

* Corresponding authors.
E-mail addresses: sjf15005@mail.ustc.edu.cn (J. Shan), pfwang5@ustc.edu.cn (P. Wang).

https://doi.org/10.1016/j.mechmat.2019.103220
Received 19 June 2019; Received in revised form 8 October 2019; Accepted 22 October 2019
Available online 24 October 2019
0167-6636/

micro plane fracture (Bažant and Kim, 1979, 1985, 1986; Horii and Nemat-Nasser, 1986). Their strengths were proved to be intermediate-stress sensitive (Handin et al., 1967; Mogi, 1967, 1971). However, corresponding discussions of dynamic loading are sparse and insufficient (Frew et al., 2010), it is significant to reveal the stress triaxiality of concrete-like materials under dynamic loading.

There are two main techniques employed to reveal the dynamic responses of concrete under triaxial confinement, i.e. the active confining pressure method and the passive confining pressure method. The active confining pressure method, in which a high-pressure hydraulic vessel is added to the uniaxial loading testing system, had been the widely used technique in the past (Christensen et al., 1972; Gran et al., 1989; Gary and Bailly, 1998; Frew et al., 2002). Gran et al. (1989) employed an explosively driven triaxial loading device to load the limestone-aggregate concrete specimens (i.e. with length 300 mm and diameter 150 mm) in dynamic triaxial compression states. The radial pressure was determined by averaging three quartz piezoelectric gauges, and the axial and circumferential strains were measured by the foil strain gauges (i.e. with length 100 mm) bonded to the middle surface of specimens. The confinement levels and the strain rates ranged respectively from zero to 124 MPa and from 0.5 s^{-1} to 10 s^{-1}. No rate effects were observed at strain rate 0.5 s^{-1}, but at strain rate 6 s^{-1}, the elastic modulus and the strength increased evidently. Employing similar apparatus, HB et al. (1999) had investigated dynamic behaviors of two granites (i.e. with length 60 mm and diameter 30 mm) at stain rates ranging from 10^{-4} s^{-1} to 10^{0} s^{-1} and with confining pressures ranging from 20 MPa to 170 MPa. Adding a high-pressure oil vessel to Kolsky bar apparatus, Frew et al. (2010) had studied the impact behavior of Indiana limestone at stain rates 10^{2} s^{-1} and 4×10^{2} s^{-1} and under confining pressures ranging from 100 MPa to 400 MPa. However, the technique cannot provide the high pressures required for compaction (Forquin et al., 2008; Forquin et al., 2010), and it is difficult to accurately measure the real-time fluctuations of lateral confining pressures in the process of axially impacting (Zhang and Zhao, 2014; Xu et al., 2015).

The passive confining pressure method, fulfilled by adding a lateral confinement ring around specimen combined with the split Hopkinson bar device (SHPB), is a newly developed technique and has been widely used in recent years. A broad range of materials combined with special structure designing and methods, involving ceramics with a shrink-fit metal sleeve (Chen and Ravichandran, 1996; 1997), concretes with large diameter bar (Forquin et al., 2007; 2008), dry sand with different rings (Song et al., 2009), concretes with the rings made of different materials and dimensions (Bailly et al., 2011), quartz sands with alumina ring and using the single-pulse loading method (Huang et al., 2013; 2014), micron-sized Silicon Carbide (SiC) powders with digital image correlation (DIC) method (Huang et al., 2016a), single-crystal Silicon with simultaneously x-ray phase contrast imaging (XPCI) and Laue diffraction method (Huang et al., 2016b), and concretes with coarse aggregates (e.g. lime-stone or siliceous, Piotrowska et al., 2016), were employed. An extensive introduction of the passive confining pressure method can refer to Chen and Song (2011). Some special treatments should be made to reduce the influence of the interface between the specimen and the ring. The radial strains were measured with several strain gauges bonded to the outer surface of the ring, and load path effects could be investigated. Since concrete-like materials showed geometry-dependent strain-rate sensitivity, the ring could considerably reduce the radial displacement, and the lateral inertia should be confined to some extent (Forquin et al., 2008). The technique is simpler and easier to be operated, but it is difficult to obtain a relative constant confining pressure during axially impacting.

Zhang and Zhao (2014) had conducted a detailed overview on these two techniques, and the experimental results had provided profound understandings of dynamic triaxial compression behaviors of concrete-like materials. When three principal stresses given by the orthogonally triaxial system demonstrated in Fig. 1 are respectively σ_x, σ_y, and σ_z, and $\sigma_x > \sigma_y$ and σ_z, the stress state provided by these two techniques is $\sigma_y = \sigma_z$. Load-paths of the intermediate-stress sensitivity cannot be analyzed, and only some special load-paths are involved in.

Special efforts had been made to achieve the true triaxial stress state (i.e. $\sigma_x \neq \sigma_y \neq \sigma_z$) on the specimens. In order to obtain the dynamic behaviors in two-axial stress state, Hummeltenberg et al. (2012) had put forth to employ two orthogonal SHPB sets to simultaneously strike the specimen, but no experimental data had been reported due to the difficulty of synchronicity between these two SHPB sets. To avoid the difficulty of synchronicity, Cadoni and Albertini (2011); Cadoni (2013); Zhao et al. (2013) had put forward a new experimental formulation that the specimen was initially loaded to be under true triaxial stress states, and then impact the specimen in certain direction by means of the SHPB method. Cadoni et al. (2015) had suggested a 3D modified Hopkinson bar (3D-MHB) with one pre-tensioned round input bar and five square output bar. This idea provides a preliminarily alternative approach for the biaxial or triaxial simultaneous impacting, which might have certain theoretical significance in physical dynamics. Cui et al. (2019) had newly developed a 3D-SHPB device that could compress the specimen synchronically in three mutually perpendicular directions with equal amplitude, and volumetric properties of concrete under dynamic hydrostatic pressure were obtained to preliminarily investigate the equation of state (EOS) of saturated concretes. The present experimental apparatus was built under the supervisor of Prof. Jian Zhao of Monash University, and some preliminarily results during apparatus installing and commissioning could refer to Refs. Xu et al. (2016, 2017, 2018).

In the present study, an effort is made to extend this experimental formulation to apply the true triaxial stress state (i.e. $\sigma_{x\text{-static}} \neq \sigma_{y\text{-static}} \neq \sigma_{z\text{-static}}$) on the specimen by three independently servo- controlled hydraulic cylinders and to produce axial impact loading by using a modified SHPB device especially designed for this purpose. The data processing method is then proposed, and as an example, dynamic behaviors (e.g. the strain rate effect, the load path effect, the intermediate stress effect, etc.) of a concrete are investigated experimentally.

2. Dynamic testing system of concrete under true triaxial static confinement

2.1. Testing principles

Testing principles in this study are schematically presented in Fig. 1. The key of the testing system is to record the dynamic responses of six surfaces of the cubic specimen during the axially impacting. As shown in Fig. 1a, the cubic specimen is positioned by six steel square bars, and the true triaxial stress state ($\sigma_{x\text{-static}} \neq \sigma_{y\text{-static}} \neq \sigma_{z\text{-static}}$) is firstly applied on the specimen by means of these six bars. And then, the striker is launched to impact the incident bar along the x-axis. An elastic incident wave (ε_i) is generated and propagates along the incident bar. When the incident wave travels to the interface of the incident bar and the cubic specimen, part of the incident wave is reflected as a reflected wave (ε_r) in the incident bar due to their impedances mismatch, and part of the incident wave is transmitted as a transmission wave (ε_t) along the impact direction. Due to lateral expanding (i.e. the Poisson effect) caused by x-axial impacting, four waves, e.g. $\varepsilon_{y\text{-}left}$, $\varepsilon_{y\text{-}right}$, $\varepsilon_{z\text{-}up}$, and $\varepsilon_{z\text{-}down}$, are generated respectively in four steel square bars, which compressed firmly with four lateral surfaces of the cubic specimen. Corresponding static confinement and dynamic stresses applied on the cubic specimen are demonstrated in Fig. 1b. It merits attention that the effect of tractions between the specimen and the lateral bar could be ignored, which further discussed in Appendix A and the results show that the actions of tractions on the overall stress equilibrium along the impact direction are transient and at local.

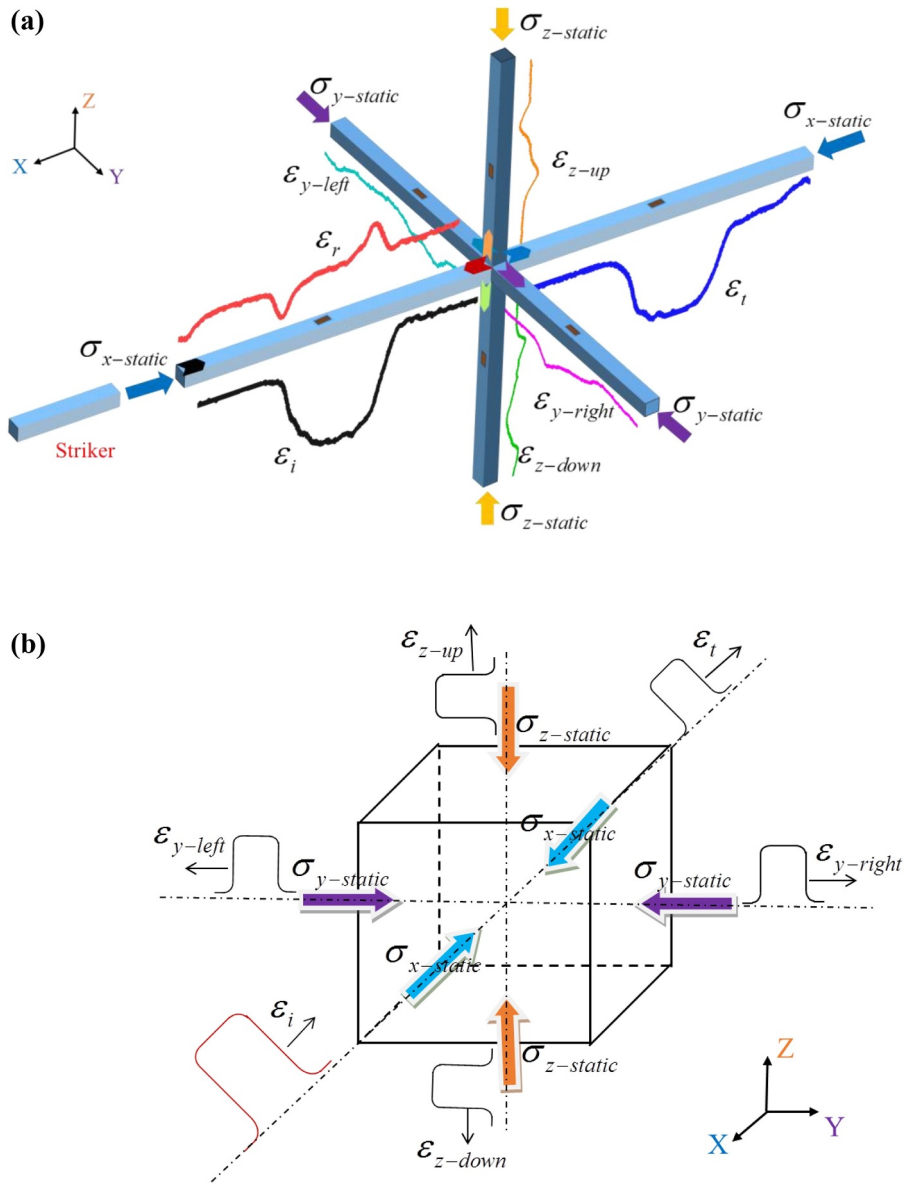

Fig. 1. Schematic diagrams of testing principle, (a) static confinement and dynamic stresses in the bars, (b) static confinement and dynamic stresses on the specimen.

2.2. Testing apparatus

Fig. 2 schematically presents the testing apparatus based on testing principle illustrated in Fig. 1. The testing apparatus is mainly composed of two testing systems, i.e. the true triaxial confinement system and the impact loading system. To describe the testing apparatus clearly, an orthogonally triaxial system is formed as shown in Fig. 2a. The x-axis and the y-axis parallel to the horizontal ground and are respectively along and vertical to the impact direction, and the z-axis is vertical to the horizontal ground.

Along the x-axis, there are in turns the high pressure gas gun (I), the cylindrical striker (II), the incident square bar (III), the cubic specimen, the transmission square bar (IV), the hollow servo-controlled hydraulic cylinder (V), the cylindrical absorption bar (VI), and the momentum trap (VII). Among them, the incident bar, the specimen, the transmission bar, and the servo-controlled hydraulic cylinder are constrained by the x-axis steel frame, static confinement in x-axis ($\sigma_{x\text{-static}}$) could be applied by pumping the hydraulic cylinder (V). The cylindrical striker impacts the incident square bar through a pre-designed hole in the steel frame. The cylindrical absorption bar contacts with the transmission bar through the hole in the hollow servo-controlled hydraulic cylinder, and delivers part of the transmission wave to the momentum trap. In the present study, the specimen is a cube with 50 mm in length, the cylindrical striker is 42 mm in diameter and 500 mm in length, the incident bar and the transmission bar are respectively 2500 mm and 2000 mm in length and their square section is 50 mm in length, and the cylindrical absorption bar is 42 mm in diameter and 800 mm in length.

Along the y-axis, there are in turns the right square bar (VIII), the cubic specimen, the left square bar (IX), and the servo-controlled hydraulic cylinder (X). They are constrained by the y-axis steel frame, and the static confinement in the y-axis ($\sigma_{y\text{-static}}$) is applied by pumping the hydraulic cylinder (X). Along the z-axis, there are in turns the up square bar (XI), the cubic specimen, the down square bar (XII), and the servo-controlled hydraulic cylinder (XIII). They are constrained by the z-axis steel frame, and the static confinement in the z-axis ($\sigma_{z\text{-static}}$) is applied by pumping the hydraulic cylinder (XIII). Lengths of four lateral bars are designed to ensure the complete wave profiles can be recorded when the length of the striker is 500 mm. In the present study, the right bar and the left bar along the y-axis are 2000 mm in length and square section with 50 mm in length, and the up bar and the down bar along

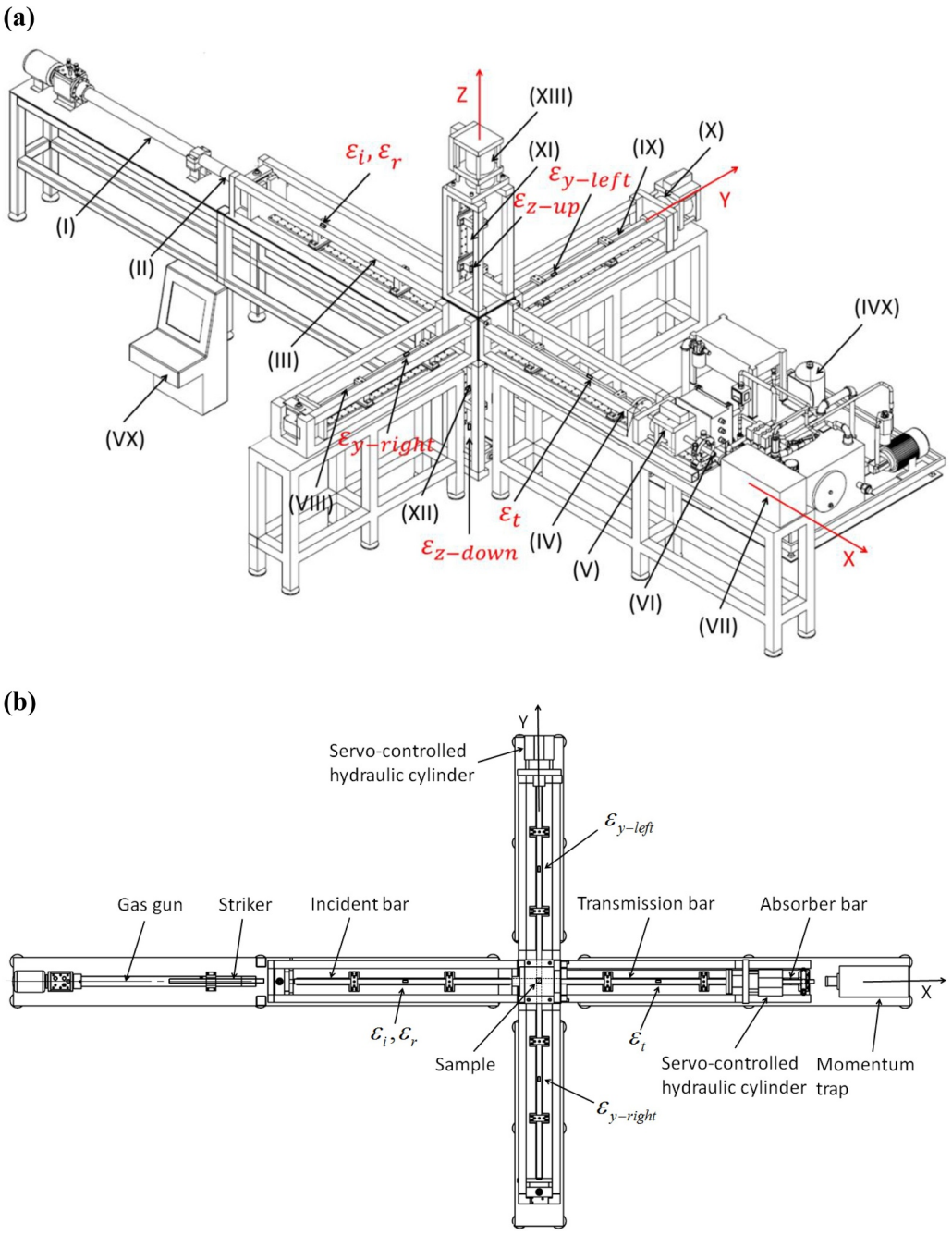

Fig. 2. Schematic diagrams of testing apparatus, (a) three dimensional graph, (b) cross section in the XY plane.

the z-axis are 1600 mm in length and square section with 50 mm in length.

These three hydraulic cylinders, e.g. cylinder (V), cylinder (X), and cylinder (XIII), are pumped by the hydraulic pump station (IVX), which independently servo-controlled by the control system (VX). The design load of each hydraulic cylinder is 600 kN, which corresponds to a maximum confinement of 240 MPa applied on the specimen.

2.3. Testing procedures

Length of the cubic specimen is machined to be a little larger than 50 mm, e.g. 50.2 mm, to avoid extruding of these six bars in the process of applying the true triaxial confinements. Surfaces of the cubic specimen are lubricated slightly by vaseline to reduce end faces friction and be helpful for wave transmission.

The testing procedure involves mainly two stages: applying the true triaxial confinements and impacting the specimen. During the first stage and taking the confinement condition $\sigma_{x\text{-static}} > \sigma_{y\text{-static}} > \sigma_{z\text{-static}}$ as example, three hydraulic cylinders are firstly pumped simultaneously to apply confinements on the specimen at a constant stress rate, e.g. 0.05 MPa/s. When the confining pressure in the z-axis (σ_z) reaches $\sigma_{z\text{-static}}$, cylinder (XIII) is hold and σ_z keeps constant, and the other cylinders continue pumping simultaneously to increase the confinements $\sigma_{y\text{-static}}$ and $\sigma_{x\text{-static}}$. Once the confining pressure in the y-axis (σ_y) reaches $\sigma_{y\text{-static}}$, cylinder (X) is hold and σ_y keeps constant. Cylinder (V) continues pumping until the confining pressure in the x-axis (σ_x) reaches $\sigma_{x\text{-static}}$. In the pumping process, σ_z and σ_y should be respectively higher than $\sigma_{z\text{-static}}$ and $\sigma_{y\text{-static}}$ due to the Poisson effect. The servo-controlled system should start work instantaneously and control the hydraulic pump station (IVX) to adjust the confining pressures to the

desired values. And then, three hydraulic cylinders are hold and the system is waiting for the next step.

At the second stage, the striker is launched at desired velocity to impact the impact bar along the x-axis. The impact velocity is measured by two lights (e.g. lasers) and time trigs. The square or circle pulse shapers, made of rubber, are used to increase duration of loading wave profiles and to adjust loading strain rate (Frew et al., 2002), which provide enough time for waves traveling over the specimen to achieve the stress equilibrium (Nemat-Nasser et al., 2005; Chen and Song, 2011). As mentioned in Section 2.1 and shown in Fig. 1, there are seven wave profiles generated during the x-axial impacting. Among them, the wave profiles of ε_i and ε_r are measured by strain gauges on the incident bar, ε_t is measured by strain gauges on the transmission bar, and $\varepsilon_{y\text{-}left}$, $\varepsilon_{y\text{-}right}$, $\varepsilon_{z\text{-}up}$, and $\varepsilon_{z\text{-}down}$ are respectively measured by strain gauges on the corresponding lateral bars shown in Figs. 1 and 2. These signals are recorded by three high-speed digital oscilloscopes, i.e. Tektronix MDO4104C. The instant information of lateral confinements is recorded by the control system. More details could be referred to Liu et al. (2019).

3. Concrete specimen and data processing

3.1. Concrete specimen

Physical and mechanical properties of concrete specimens depend on the coarse aggregates (e.g. siliceous gravels or limestone-crushed aggregates) (Piotrowska et al., 2014). The selected concrete in the present study is a commercial intermediate-strength concrete with limestone crushed aggregates. Concrete blocks with size $150 \times 150 \times 150\,mm^3$ are cast by using commercial concrete, and then cured in moist environment for over 30 days. The composition and the mechanical properties are summarized in Table 1. The testing specimens illustrated in Table 2 are machined from these concrete blocks.

3.2. Loading pulse and incident waveform

Formation and propagation of the loading pulse in the present testing system is somewhat different from the conventional SHPB tests. As shown in Fig. 3, formation of the pulse includes two stages. At stage I, the striker impacts the incident bar constrained by the x-axis steel frame. The static confinement force ($F_{\text{x-static}}$) is the inner force in the bar-frame system, and it does not act on the striker. The x-t diagram of stage I is shown in Fig. 3a, and state of the interface of the striker and the bar corresponds to state (3) shown in the impact force-particle velocity (F-v) diagram of Fig. 3c. At stage II, once the impact bar is compressed and detaches from the steel frame, the static confinement force ($F_{\text{x-static}}$) is released and become a new disturbance source propagating to the interface of the striker and the bar. From state (3) to state (4), there is a jump with amplitude $F_{\text{x-static}}$ corresponding to the disturbance source at the beginning of stage II. The corresponding x-t diagram is shown in Fig. 3b, and state of the interface of the striker and the bar at stage II corresponds to state (6) shown in the F-v diagram of Fig. 3c. The final states of the striker and the bar are state (7) and state (8), respectively. A loading pulse with duration $2\chi/C_0$ (here, χ and C_0 are respectively length and wave velocity of the striker), which similar with the conventional SHPB tests, is then formed. The striker would rebound with higher speed than that of the conventional SHPB test.

Fig. 3d illustrates the incident waveforms measured at the middle surface of the impact bar by strain gauges. The loading part of the incident wave is similar with the conventional SHPB tests, but the unloading part is different, in which their amplitudes increase with increasing the static confinements in the x-axis. The extra amplitudes are close to the x-axial confinements, e.g. 30 MPa, 45 MPa, and 60 MPa. In the process, the bar could be taken to be particle chain that composed of a string of particles along the direction of wave propagation. When the unloading wave arrives, the particles compressed in the loading process are released in turn to be free. Since the static confinement is applied on the ends of the incident bar and the transmission bar by the hydraulic cylinder and the steel frame, rather than applied directly on the measuring point that strain gauge stuck to, the local loading stresses including the dynamic stress and the confining pressure are released thoroughly when the unloading wave arrives. At the same time, the static confinement delivers gradually from the hydraulic cylinder to the measured surface along the particle chain with increasing time. The process is illustrated by curve ABC in Fig. 3d, and it takes several milliseconds for the unloading curve approaching to the baseline.

Table 1
Composition and mechanical properties of concrete.

Compositions	
Water(kg/m^3):	185
Cement(kg/m^3):	429
Sand (kg/m^3):	
Medium sand with fineness modulus 2.94	536
Coarse aggregates (kg/m^3):	
With continuously distributed particles diameter: 5–31.5 mm	1250
Mean Density (kg/m^3):	2392
Mechanical properties	
Compressive strength *(MPa):	38
Tensile strength (MPa):	1.0–2.0
Poisson's ratio	0.21

Note: * denotes compressive strength of a cubic specimen with length 150 mm.

3.3. Wave profiles

Typical wave profiles under true axial confinements are shown in Fig. 4. Along the x-axis, the wave profiles of ε_i, ε_r, and ε_t are illustrated and analyzed by the three-wave method (Chen and Song, 2011), as demonstrated at right top in Fig. 4a. Although there are four lateral confining bars and part of the effects of x-axial impacting should be shared by these four bars, stress equilibrium along the x-axis is achieved to some extent. Along the y-axis, the wave profiles of $\varepsilon_{y\text{-}left}$ and $\varepsilon_{y\text{-}right}$ are illustrated and analyzed as showed at top right in Fig. 4b. These two wave profiles are almost the same but with much lower amplitudes, and the stress equilibrium between the right side and the left side of the specimen is achieved during the x-axis impacting. As illustrated in Fig. 4c, similar conclusion could be reached along the z-axis.

3.4. Data processing method

The stress on the specimen is the sum of the static confining pressure and the dynamic stress (the stress disturbance), i.e. in the x-axis, $\sigma_x = \sigma_{\text{x-static}} + \sigma_{\text{x-dyn}}$. The static confining pressures are calculated by the actual confinements. According to the waveforms shown in Fig. 4, the dynamic stresses could be independently calculated. In the x-axis, the dynamic stress ($\sigma_{\text{x-dyn}}$) is calculated based on two assumptions, e.g. the one-dimensional stress wave assumption and the stress equilibrium assumption, as presented in the conventional SHPB tests (Chen and Song, 2011). In the y-axis and the z-axis, their dynamic stresses ($\sigma_{\text{y-dyn}}$ and $\sigma_{\text{z-dyn}}$) are calculated respectively based on their force equilibriums of two opposite surfaces of the specimen in corresponding direction during the x-axially impacting, e.g. in the y-axis, $F^{left}_{y-dyn}(t) = E_0 A_0 \varepsilon_{y-left}(t)$ on the left end, $F^{right}_{y-dyn}(t) = E_0 A_0 \varepsilon_{y-right}(t)$ on the right end, and $F^{left}_{y-dyn}(t) = F^{right}_{y-dyn}(t)$ on the specimen (here, A_0 and E_0 are respectively the area and the elastic modulus of the square bar).

Similar with the conventional SHPB tests, the strain rate ($\dot{\varepsilon}_{x-dyn}$), the strain ($\varepsilon_{x-dyn}$), and the dynamic stress (σ_{x-dyn}) in the x-axis are expressed as follows.

$$\dot{\varepsilon}_{x-dyn}(t) = \frac{C_0}{L_{s-\text{X}}}[\varepsilon_i(t) - \varepsilon_r(t) - \varepsilon_t(t)] \tag{1}$$

Table 2
Summary of dynamic experiments of cement samples.

Sample No	Impact velocity (m/s)	Strain rate (s^{-1})	Sample size (mm)			Confining pressure (MPa)			Dynamic pressure (MPa)			Remarks
			x*	y	z	x	y	z	x	y	z	
1	9.7	~50	49.98	50.02	50.02	0.0	0.0	0.0	44.6	0.0	0.0	Failed
2	13.3		50.04	49.90	50.14	0.0	0.0	0.0	93.5	13.5	0.0	Failed
3	13.1		50.04	50.16	50.06	7.5	7.5	7.5	104.7	13.1	11.3	cracks
4	13.2		49.92	50.24	50.22	15.0	7.5	7.5	109.3	14.1	14.0	cracks
5	13.0		49.36	50.50	50.26	30.0	7.5	7.5	99.0	14.1	16.6	cracks
6	21.9		50.06	50.10	50.10	45.0	45.0	45.0	216.2	18.3	20.2	cracks
7	22.3		50.04	50.36	50.24	45.0	7.5	7.5	204.1	36.2	19.5	cracks
8	14.2		50.62	50.62	50.78	30.0	0.0	30.0	90.0	0.0	7.52	Fractured
9	13.7		50.46	50.56	50.40	45.0	0.0	45.0	74.7	0.0	4.0	Fractured
10	13.8		50.20	50.14	50.10	16.0	12.0	16.0	140.0	14.9	16.0	cracks
11	13.7		50.00	50.24	50.20	12.0	12.0	20.0	148.3	13.8	16.5	cracks
12	13.8		49.94	50.28	50.23	12.0	12.0	40.0	153.7	15.8	16.5	cracks
13	13.8		49.90	50.30	50.24	12.0	12.0	60.0	153.7	16.4	12.4	cracks
14	13.0	~100	49.96	50.02	50.00	0.0	0.0	0.0	74.7	0.0	0.0	Failed
15	13.2		50.06	50.04	50.06	7.5	7.5	0.0	80.0	11.5	0.0	Failed
16	21.6		50.04	50.10	49.94	30.0	7.5	7.5	202.7	24.2	22.8	cracks
17	27.2		49.78	50.14	50.24	30.0	7.5	7.5	246.0	46.6	43.6	cracks
18	21.8		50.66	50.64	50.60	60.0	60.0	60.0	174.0	15.2	15.3	cracks
19	22.0		50.36	50.70	50.88	60.0	30.0	60.0	186.4	21.8	17.6	cracks
20	22.0		50.32	50.90	50.94	60.0	12.5	60.0	163.0	40.3	16.0	cracks
21	22.0		50.78	50.66	50.78	30.0	30.0	30.0	186.2	20.1	16.6	cracks
22	21.5		50.42	50.70	50.72	30.0	30.0	7.5	175.5	32.3	26.1	cracks
23	20.4		50.38	50.50	50.26	5.5	2.8	3.9	191.7	24.4	26.1	cracks
24	20.8		50.32	50.54	50.38	0.0	0.0	0.0	192.5	26.5	29.4	Fractured
25	20.8		50.64	50.42	50.12	7.5	7.5	7.5	177.8	21.5	23.0	cracks
26	20.3		49.94	50.52	50.50	30.0	0.0	30.0	93.7	0.0	6.8	Fractured
27	21.5		50.00	50.10	50.10	12.0	4.0	12.0	181.3	43.1	40.7	cracks
28	22.5		49.98	50.24	50.14	20.0	4.0	20.0	174.8	33.2	32.6	cracks
29	14.9		50.00	50.10	49.70	12.0	0	12.0	138.3	0.0	15.2	Failed
30	21.5		50.00	50.10	50.10	12.0	12.0	8.0	170.3	38.7	32.3	cracks
31	22.5		49.87	50.14	50.24	40.0	40.0	8.0	185.3	44.0	44.0	cracks
32	22.3		49.82	50.18	50.30	40.0	60.0	8.0	192.5	46.8	34.2	cracks
33	22.3		49.80	50.19	50.35	60.0	80.0	8.0	210.5	35.5	44.0	cracks
34	22.2		49.75	50.20	50.40	32.0	0.0	60.0	175.0	38.7	33.2	Failed
35	13.7		49.80	50.50	50.28	0.0	0.0	60.0	143.0	0.0	5.2	cracks
36	13.6		49.78	50.54	50.30	0.0	0.0	40.0	142.2	0.0	4.8	Fractured
37	29.0	~200	50.56	50.54	50.16	7.5	7.5	7.5	236.0	45.2	45.4	cracks
38	32.6		50.36	50.50	50.42	45.0	45.0	45.0	244.4	38.2	42.7	cracks
39	31.5		50.20	50.60	50.78	45.0	7.5	45.0	257.9	58.0	44.7	cracks
40	30.9		50.60	50.62	50.40	60.0	60.0	60.0	251.1	34.4	33.6	cracks
41	28.7		50.40	50.68	50.62	60.0	30.0	60.0	238.1	47.3	19.5	cracks
42	23.0		50.08	50.40	50.30	30.0	0.0	30.0	115.9	0.0	12.6	Fractured
Static1		10^{-3}	50.10	49.98	50.04	0.0	0.0	0.0	66.0	0.0	0.0	Failed
Static3			50.24	50.44	50.52	0.0	0.0	0.0	65.1	0.0	0.0	Failed
Static2		10^{-4}	50.10	50.06	50.20	0.0	0.0	0.0	64.5	0.0	0.0	Failed
Static4			50.40	50.26	50.32	0.0	0.0	0.0	65.2	0.0	0.0	Failed
43	13.3	<20	50.0	50.04	50.06	7.5	12.5	0.0	147.0	8.35	0.0	Fractured
44	8.1		50.76	50.50	50.58	30.0	0	30.0	50.6	0.0	1.2	cracks
45	10.4		50.68	50.60	50.72	30.0	0	30.0	80.0	0.0	3.0	cracks

Note: * "x", "y", and "z" denote x-direction, y-direction, and z-direction shown in Fig. 1, respectively.

$$\varepsilon_{x-dyn}(t) = \frac{C_0}{L_{s-\mathrm{X}}}\int_0^t [\varepsilon_i(t) - \varepsilon_r(t) - \varepsilon_t(t)]dt \tag{2}$$

$$\sigma_{x-dyn}(t) = \frac{A_0}{2A_{s-\mathrm{X}}}E_0[\varepsilon_i(t) + \varepsilon_r(t) + \varepsilon_t(t)] \tag{3}$$

where, C_0 is the wave velocity of the bars, and $L_{s\text{-}x}$ and $A_{s\text{-}x}$ are respectively the length and the area in the x-axis for the specimen.

Taking into account the differences of forces applied on two opposite surfaces of the specimen, the load applied on the specimen is calculated by averaging the forces of the opposite surfaces. The strain rate ($\dot{\varepsilon}_{x-dyn}$), the strain ($\varepsilon_{k-dyn}$), and the dynamic stress (σ_{k-dyn}) in the y-axis and the z-axis are expressed as follows.

$$\dot{\varepsilon}_{k-dyn}(t) = \frac{|\Delta v|}{L_{s-k}} = \frac{C_0|\varepsilon_{k1}(t) + \varepsilon_{k2}(t)|}{L_{s-k}} \tag{4}$$

$$\varepsilon_{k-dyn}(t) = \frac{C_0}{L_{s\_k}}\int_0^t [\varepsilon_{k1}(t) + \varepsilon_{k2}(t)]dt \tag{5}$$

$$\sigma_{k-dyn}(t) = \frac{A_0}{2A_{s\_k}}E_0[\varepsilon_{k1}(t) + \varepsilon_{k2}(t)] \tag{6}$$

where, k denotes the y-axis or the z-axis, and $L_{s\text{-}k}$ and $A_{s\text{-}k}$ are respectively the length and the area in the k-direction (y-axis or z-axis) for the specimen. Δv is the velocity difference between the opposite surfaces in the k-direction. ε_{k1} and ε_{k2} are respectively $\varepsilon_{y\text{-}left}$ and $\varepsilon_{y\text{-}right}$ when k denotes y-axis, and respectively $\varepsilon_{z\text{-}up}$ and $\varepsilon_{z\text{-}down}$ when k denotes z-axis.

When the tractions between the specimen and the lateral bars are taken into account, the data processing method is demonstrated in Appendix A.

4. Results

4.1. The dynamic stress-strain relationship

The lateral confinement had evident effects on the failure patterns and the stress-strain relationships. Fig. 5a illustrates the dynamic

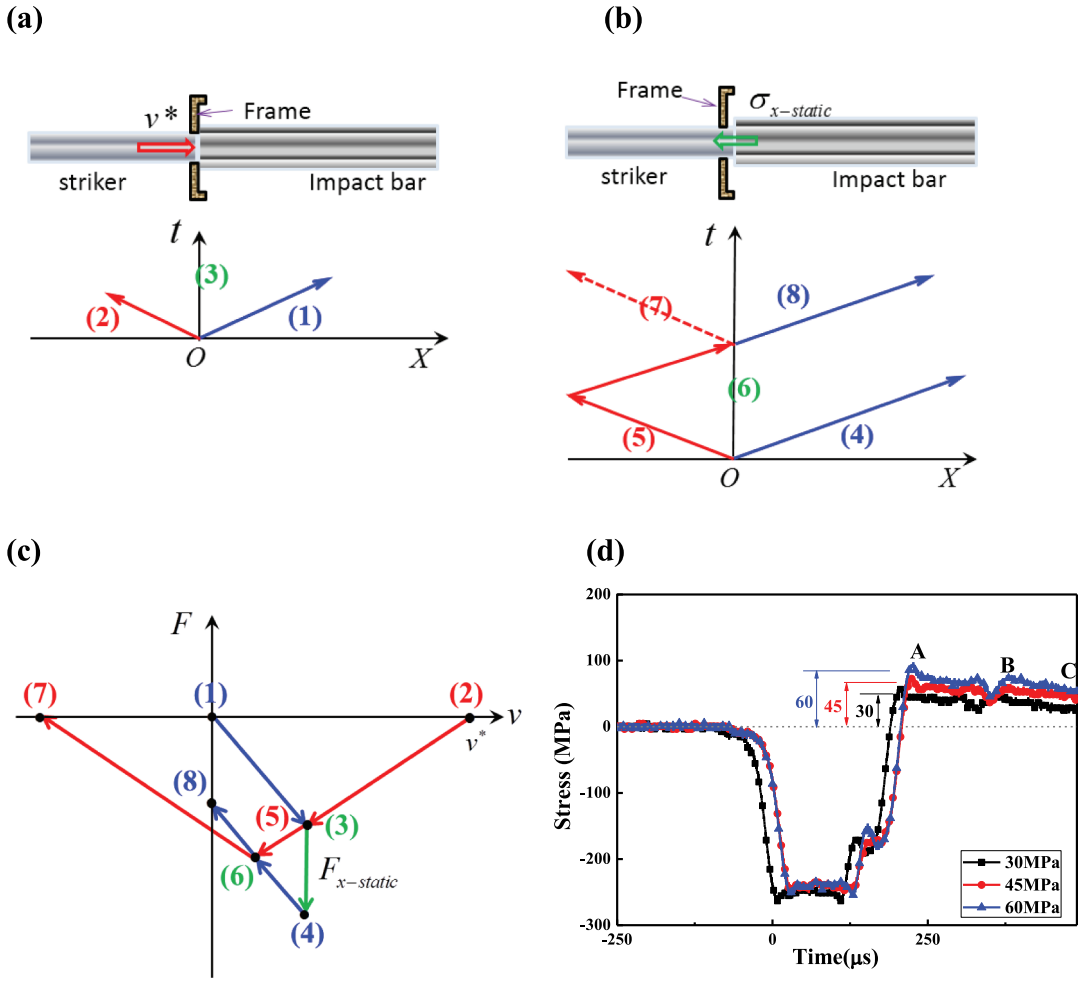

Fig. 3. Formation and propagation of loading pulse in the impact/incident bar. (a) stage I; (b) stage II; (c) F-v diagram; (d) Incident waveforms in the middle part of the impact/incident bar recorded by strain gauge (Impact velocity is 19 m/s).

engineering stress- engineering strain relationships of specimens under three confinement conditions. Under uniaxial dynamic compression and with no lateral confinement e.g. [$\sigma_{x\text{-static}}$; $\sigma_{y\text{-static}}$; $\sigma_{z\text{-static}}$] = [0;0;0], the specimen is failed into fragments, and the dynamic stress-strain relationship shows lower strength and very small strain, i.e. smaller than 0.5%. Under biaxial lateral confinements [30;0;30], which with unit MPa and hereinafter, the specimen is impacted to be interfacial delamination along the unconfined surface, and the dynamic stress-strain relationship in the x-axis shows higher strength and intermediate strain, e.g. 1.0%. Under triaxial lateral confinements [30;30;30], there are some meso cracks observed to be evenly distributed at local in the specimen, but with no macro failure. The dynamic engineering stress- engineering strain relationship in the x-axis shows higher strength and larger strain, e.g. 1.8%, and takes on plastic hardening properties. With increasing the lateral confinements, failure pattern of concrete turns gradually from the brittle failure mode to the ductile failure mode. As illustrated in Fig. 5b, the lateral stress-strain relationships in the y-axis and the z-axis of specimen under triaxial lateral confinements are similar, and they show larger lateral strain than that of specimen under biaxial lateral confinements.

Fig. 6 demonstrates the dynamic engineering stress- engineering strain relationships of specimens under biaxial lateral confinements [30;0;30] and at three impact velocities, i.e. 8.10, 10.35, and 14.23 m/s. The strengths in the x-axis increase with increasing the impact velocity. The specimens are not failed when the impact velocity lower than 10.35 m/s, and failed when the velocity up to 14.23 m/s. The x-axis strain rate is evaluated based on Eq. (1) and listed in the bracket shown in Fig. 6a, and corresponding lateral strain rates in the y-axis and the z-axis are evaluated based on Eq. (4) and listed in the bracket shown in Fig. 6b. The lateral engineering stresses and engineering strains are measured to be with lower values, and increase with increasing the x-axial impact velocity. The lateral strain rate is relatively lower than that in the impact direction. Therefore, the x-axis strain rate is employed in the present study to approximately describe the strain rate effect.

4.2. Relationship of volume strain and hydrostatic pressure

The concrete-like materials contain a variety of voids, e.g. macroscopic pores, mesoscopic gelatinous voids, etc. They are typical porous media and normally with porosity higher than 10% (Tang et al., 2005). Volumetric compression plays significant roles in the dynamic responses of the specimen under higher lateral confinements. Fig. 7 illustrates the relationship between the dynamic volume strain and the hydrostatic pressure. The start point, ($\varepsilon_{v\text{-static}}$, p_{static}), of the curve is calculated based on the static confinements, and could be expressed as: $p_{static} = (\sigma_{x-static} + \sigma_{y-static} + \sigma_{z-static})/3$ and $\varepsilon_{v-static} = p_{static}/K$. Here, volume modulus $K = E_s/[3(1 - 2\nu_s)]$, and E_s and ν_s are respectively the elastic modulus and Poison's ratio of the specimen. The specimen is firstly impacted under lateral confinement [60;60;60] with velocity 21.8 m/s, and then impacted under lateral confinement [60;12.5;60] with velocity 22.0 m/s. The volume strain in the first impact is small and no evident macro failures are observed due to higher triaxial confinements. Volume strain of the second impact is larger and macro fractures are observed mainly perpendicular to the y-axis, which similar

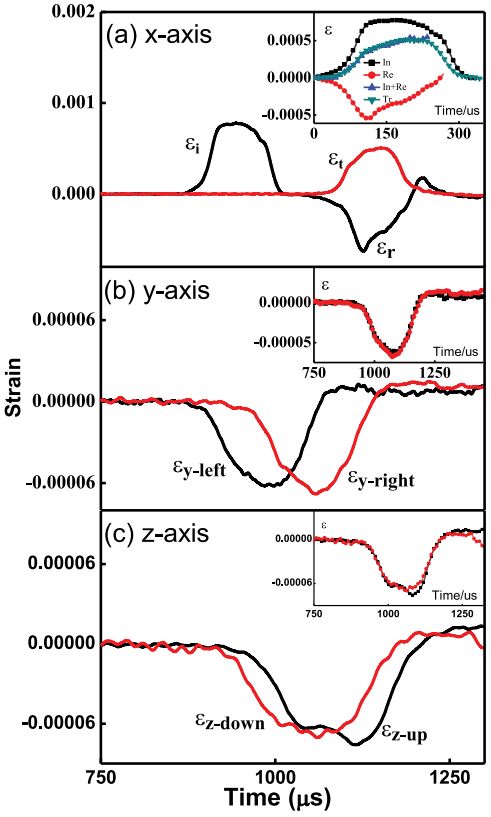

Fig. 4. Typical wave profiles along three axes.

with the middle image shown in Fig. 5a. The curve of hydrostatic pressure VS volume strain for the second impact could be roughly divided into four stages. At stage AB, it shows linear deformation property with higher modulus than the first impact, which results from the void compaction during the first impact. At stage BC, larger volume compression occurs due to void collapse. At stage CD, it shows another linear increasing tendency, and at stage DE, it shows the strain-hardening property. In the process, although the specimen under higher lateral confinements is not failed during impact, it is compressed obviously in the impact direction, and shows obvious expansion in other directions. Cracks are observed to be scattered distributed at local. Comparison of the two curves, specimen deformation and failure prone to the deviator stresses, which cause the nucleation and growth of cracks.

4.3. Relationship of equivalent strain and equivalent stress

The equivalent strain ($\bar{\varepsilon}$) and the equivalent stress ($\bar{\sigma}$) are expressed respectively as:

$$\bar{\varepsilon} = \sqrt{\frac{4}{3}J_2'} \tag{7}$$

$$\bar{\sigma} = \sqrt{3J_2} \tag{8}$$

where, J_2' and J_2 are the second invariants of the strain deviator tensor and the stress deviator tensor, respectively. In the present study, they could be expressed as:

$$J_2' = \frac{1}{6}[(\varepsilon_{x-dyn} + \varepsilon_{x-static} - \varepsilon_{y-dyn} - \varepsilon_{y-static})^2 + (\varepsilon_{y-dyn} + \varepsilon_{y-static} - \varepsilon_{z-dyn} - \varepsilon_{z-static})^2 + (\varepsilon_{z-dyn} + \varepsilon_{z-static} - \varepsilon_{x-dyn} - \varepsilon_{x-static})^2] \tag{9}$$

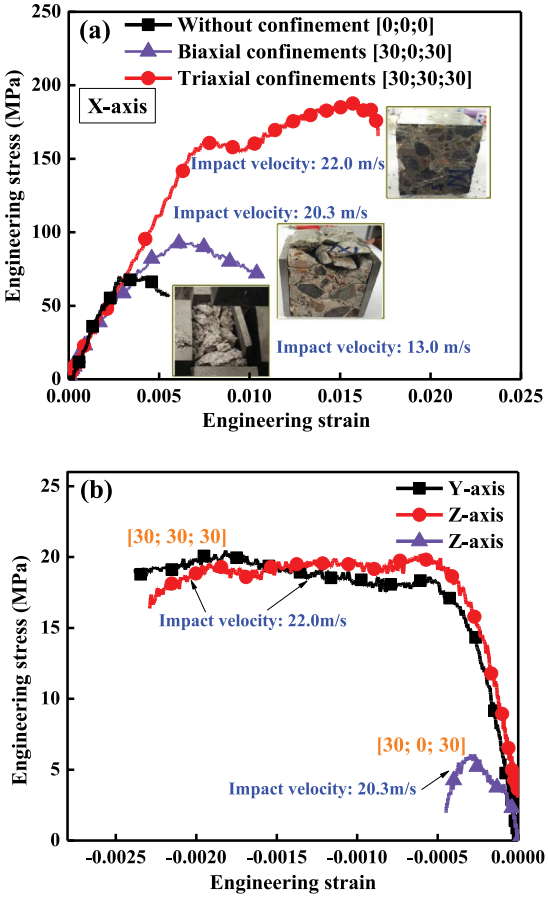

Fig. 5. Stress-strain relationship of the specimens under three confinement conditions: in the x-axis, (b) in the y-axis and the z-axis. In figure, [30;0;30] denotes that the static confinements are respectively 30 MPa in the x-axis, 0 MPa in the y-axis, and 30 MPa in the z-axis, hereinafter.

$$J_2 = \frac{1}{6}[(\sigma_{x-dyn} + \sigma_{x-static} - \sigma_{y-dyn} - \sigma_{y-static})^2 + (\sigma_{y-dyn} + \sigma_{y-static} - \sigma_{z-dyn} - \sigma_{z-static})^2 + (\sigma_{z-dyn} + \sigma_{z-static} - \sigma_{x-dyn} - \sigma_{x-static})^2] \tag{10}$$

Fig. 8a illustrates the relationship of the equivalent strain and the equivalent stress of specimens at the strain rate 50s^{-1} and under the confining pressures 7.5 MPa in both the y-axis and the z-axis. When the x-axis confinement increases from 7.5 to 30 MPa, the equivalent strength increases from 93.77 to 111.18 MPa, and the equivalent strain of peak point decreases from 0.469% to 0.315%, which caused by the increasing of pre-applied deviatoric stress. As a comparison, the relationship of the equivalent shear strain ($\bar{\gamma} = \sqrt{4J_2'}$) and the equivalent shear stress ($\bar{\tau} = \sqrt{J_2}$) is illustrated in Fig. 8b. The results are similar with those of the equivalent stress and strain.

Fig. 9a demonstrates the relationship of the equivalent strain and the equivalent stress of specimens under lateral confinements [30;0;30] and at various strain rates, i.e. 20, 50, 100, and 200 s^{-1}. Similar with the results of the conventional SHPB, the equivalent strength shows evident strain rate dependence when strain rate increasing from 20 s^{-1} to 200 s^{-1}. Similar rules could be obtained on the relationship of the equivalent shear strain and shear stress illustrated in Fig. 9b.

5. Dynamic strength

5.1. DIF

The experimental results of concrete samples subjected to impact loading at strain rates ranging from 50 to 200 s^{-1} and under true

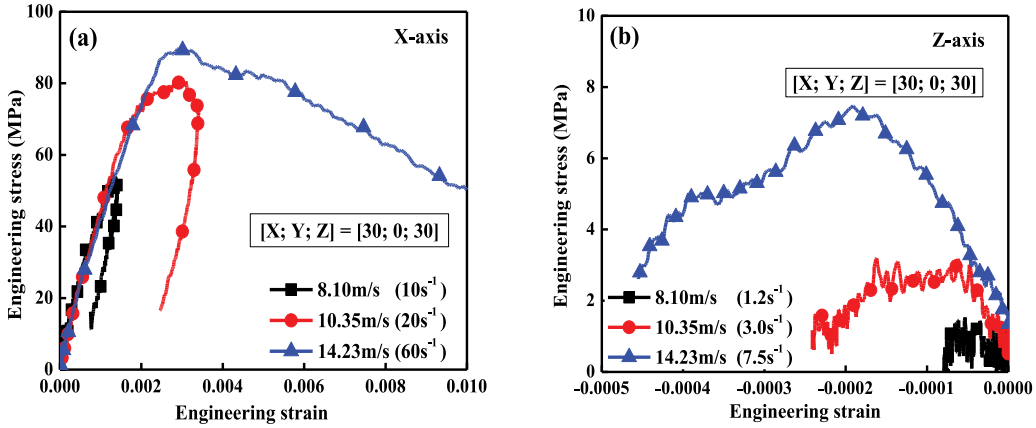

Fig. 6. Stress-strain relationship of the specimen at three impact velocities and under biaxial confinements [30;0;30], (a) in the x-axis, (b) in the z-axis.

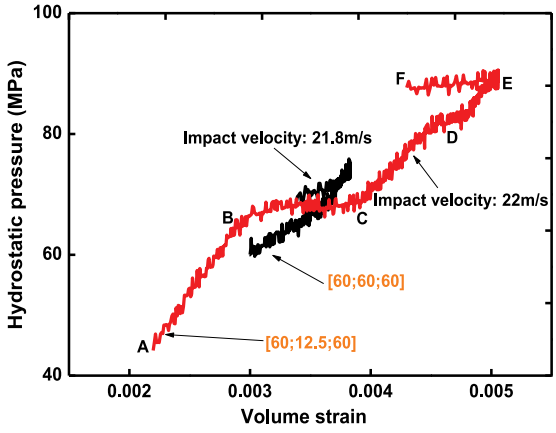

Fig. 7. Relationship of volume strain and hydrostatic pressure.

triaxial confinements ranging from 0 to 60 MPa are summarized in Table 2, and DIF results are illustrated in Fig. 10. These DIF relations demonstrated in Fig. 10 are listed in Table 3.

DIF of the equivalent strength is expressed as: DIF = $\bar{\sigma}_{cd}/\sigma_{cs}$, where $\bar{\sigma}_{cd}$ is the dynamic equivalent strength, and σ_{cs} is the uniaxial compressive strength in quasi-static loading. They take on evident strain rate dependence, and much higher than those under conventional SHPB compression. Among them, DIFs under triaxial confinements are the highest, and DIFs under uniaxial compression are the lowest. Concrete-like materials generally take on obvious strength enhancement at strain rates above a critical value between 10 and 100 s^{-1} (Li and Meng, 2003). The critical strain rate of the present study is 25.7 s^{-1}, which close to the strain rate, i.e. 30 s^{-1}, suggested by European CEB and Malvern and Ross (1985).

5.2. Dynamic triaxial strength

Zhao (2000) had employed the Mohr–Coulomb (M-C) criterion, in which the effect of loading rate to the internal friction angle was ignored, and the Hoek-Brown (H-B, Hoek and Brown, 1997) criterion, in which the effect of loading rate to parameter *m* was ignored, to describe the dynamic strength of rocks. Since the intermediate stress could not be properly dealt with in these two criterions, the Drucker-Prager (D-P) criterion is employed in the present study to describe the dynamic failure surface of concrete. The D-P criterion is a pressure-dependent model and has been widely applied to rock and concrete-like materials (Drucker and Prager, 1952; Alejano and Bobet, 2012). Although the criterion tends to overestimate the strength of intact materials (Alejano and Bobet, 2012), it is established as a generalization of the M–C criterion and easy to be used and implemented in numerical investigations. The D-P criterion in the $\sqrt{J_2} - I_1$ plane is expressed as

$$\sqrt{J_2} = \alpha_0 I_1 + k_0 \tag{13}$$

where, $I_1 = \sigma_x + \sigma_y + \sigma_z$, α_0 and k_0 are material parameters. In the present study, two stress states described by Eqs. (14) and (15) are involved in as comparison. The state described by Eq. (15) has been used in Eq. (10) to calculate the equivalent stress. While the state described by Eq. (14) denotes the results measured by the active confining pressure methods, in which the lateral confinements are taken to be constant during axially impact, and the dynamic stresses generated in the lateral surfaces of the specimen are not taken into account.

$$\sigma_X = \sigma_{x-static} + \sigma_{x-dyn},\ \sigma_Y = \sigma_{y-static},\ \sigma_Z = \sigma_{z-static} \tag{14}$$

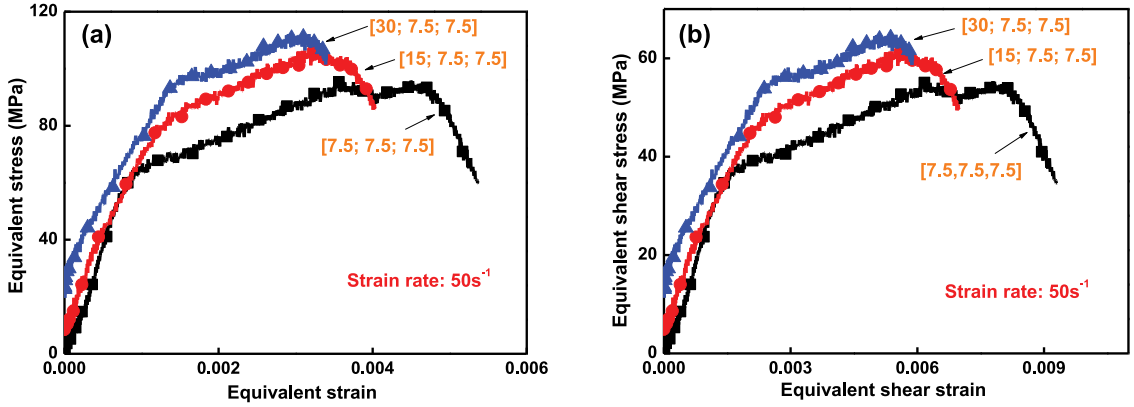

Fig. 8. The equivalent stress-strain curves at the strain rate 50 s^{-1}. (a) The equivalent stress and strain; (b) the equivalent shear stress and strain.

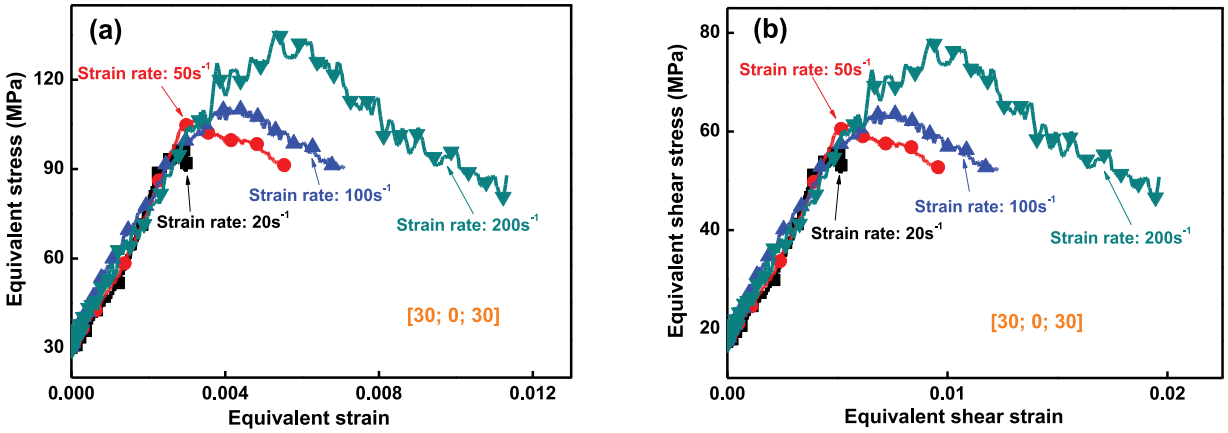

Fig. 9. The equivalent stress-strain curves at various strain rates. (a) The equivalent stress and the equivalent strain; (b) the equivalent shear stress and the equivalent shear strain.

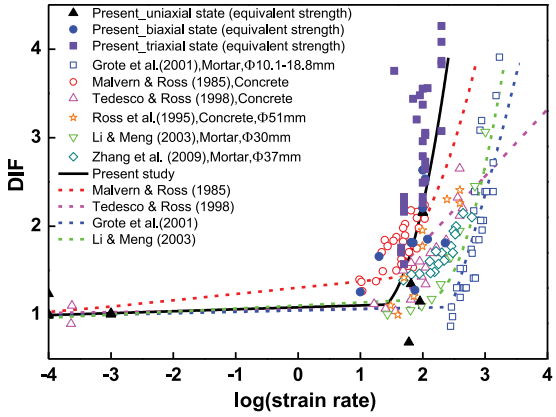

Fig. 10. DIF results and various DIF relations.

$$\sigma_X = \sigma_{x-static} + \sigma_{x-dyn},\ \sigma_Y = \sigma_{y-static} + \sigma_{y-dyn},\ \sigma_Z = \sigma_{z-static} + \sigma_{z-dyn} \tag{15}$$

The fitting results are illustrated in Fig. 11 and Table 4. The hollow marks shown in Fig. 11(a) denote the results calculated by the stress state of Eq. (14), and the solid marks denote the results calculated by the stress state of Eq. (15). Since there is no evident rate effect from the quasi-static compression to lower strain rate impacting, these data of strain rate lower than 20 s^{-1} are preliminarily classified into one group to be a reference. The difference of these two stress states increases with increasing strain rate, e.g. the ratio of the difference to the strength of the present approach increases to about 20% when the strain rate reaches 200 s^{-1}. The assumption that the lateral confinements are constant during axially impact in the active confining pressure method should lead to the overestimation of the strength, especially in the experiments at higher strain rate. These results also reveal the effect of lateral inertia on the dynamic strength.

Fig. 11(b)–(e) demonstrate the fitting results by the D-P strength criterion, and Fig. 11(f)–(i) demonstrate corresponding dynamic engineering stress-engineering strain curves, in which the load path effects and the strain rate effects have been presented in Section 4. The fitting material parameters (α_0 and k_0) are illustrated in Fig. 12(a) and Table 4. The results show that with increasing strain rate, parameter α_0 decreases, and parameter k_0 increases. Since the D–P criterion is a smoothed M–C criterion to some extent, material parameters (α_0 and k_0) could be expressed by the cohesion (c) and the friction angle (ϕ). If the D–P strength surface is assumed to be circumscribed with the M–C strength surface, the expressions could be obtained as (Alejano and Bobet, 2012):

$$\alpha_0 = \frac{2\sin\phi}{\sqrt{3}(3-\sin\phi)} \tag{16}$$

$$k_0 = \frac{6c\cos\phi}{\sqrt{3}(3-\sin\phi)} \tag{17}$$

The calculated cohesion and friction angle are demonstrated in Fig. 12(b) and Table 4. The results show that with increasing strain rate, the friction angle (ϕ) increases, and the cohesion (c) decreases. Similar

Table 3
The DIF relations.

Refs.	DIF* relations	Materials
European CEB; Malvern and Ross (1985)	$\mathrm{DIF} = \begin{cases} (\dot{\varepsilon}/\dot{\varepsilon}_s)^{1.026\alpha_s}, & \dot{\varepsilon} \le 30s^{-1} \\ \gamma_s(\dot{\varepsilon}/\dot{\varepsilon}_s)^{0.33}, & \dot{\varepsilon} > 30s^{-1} \end{cases}$ where, $\alpha_s = 1/(5+9f_{cs}/f_{co})$, $\gamma_s = 10^{(6.156\alpha_s-2)}$	concrete
Tedesco and Ross (1998)	$\mathrm{DIF} = \begin{cases} 1+0.00965(\log\dot{\varepsilon}+6.0) \ge 1, & \dot{\varepsilon} \le 63.1s^{-1} \\ 1+0.758(\log\dot{\varepsilon}-0.938) \le 2.5, & \dot{\varepsilon} > 63.1s^{-1} \end{cases}$	concrete
Grote et al. (2001)	$\mathrm{DIF} = \begin{cases} 1+0.0157(\log\dot{\varepsilon}+3.0), & \dot{\varepsilon} \le 266s^{-1} \\ 0.383(\log\dot{\varepsilon})^2+0.226\log\dot{\varepsilon}+1.765, & \dot{\varepsilon} > 266s^{-1} \end{cases}$	Mortar Φ10.1–18 mm
Li and Meng (2003)	$\mathrm{DIF} = \begin{cases} 1+0.034(\log\dot{\varepsilon}+3.0), & \dot{\varepsilon} \le 100s^{-1} \\ 1.729(\log\dot{\varepsilon})^2-7.137\log\dot{\varepsilon}+8.530, & \dot{\varepsilon} > 100s^{-1} \end{cases}$	Mortar Φ30 mm
Present study	$\mathrm{DIF} = \begin{cases} 1+0.02192(\log\dot{\varepsilon}+3.771), & \dot{\varepsilon} \le 25.7s^{-1} \\ 2.147(\log\dot{\varepsilon})^2-5.408\log\dot{\varepsilon}+4.466, & \dot{\varepsilon} > 25.7s^{-1} \end{cases}$	Concrete 50 × 50 mm

Note: *DIF = σ_{cd}/σ_{cs}, where σ_{cs} and σ_{cd} are the unconfined uniaxial compressive strength in quasi-static and dynamic loading, respectively.

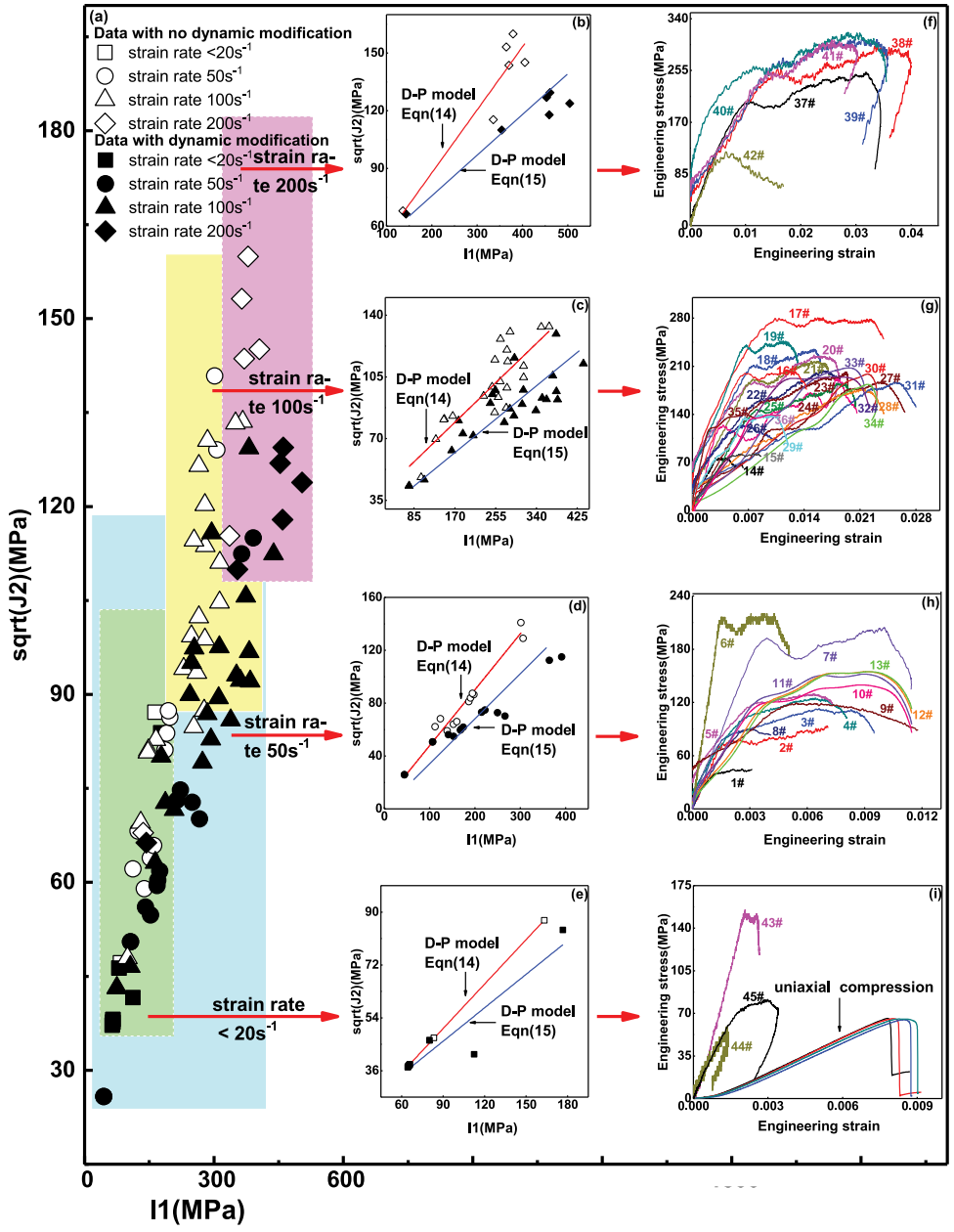

Fig. 11. The strength statistics in the $\sqrt{J_2} - I_1$ plane at various strain rates.

Table 4
Parameters of Drucker Prager strength model.

Strain rate (s^{-1})	Drucker-Prager model α_0		k_0		Cohesion, C (MPa)		Strength parameter Friction angle, ϕ (degree)	
	1*	2*	1	2	1	2	1	2
<20	0.50	0.35	4.90	13.90	7.01	12.88	65.02	44.12
50	0.41	0.26	6.87	18.20	7.27	15.42	53.10	33.46
100	0.34	0.20	19.36	28.34	16.40	23.35	45.46	26.65
200	0.32	0.18	22.00	42.58	19.70	34.88	40.60	23.74

Note: * "1" and "2" denote respectively the stress states described by Eqs. (14) and (15).

results had been reported for granite under dynamic combined compression and shear loading (Xu et al., 2015; Zhou et al., 2018). Differences between the results calculated by Eq. (14) and those calculated by Eq. (15) increase with increasing strain rate, the results show that it is significant to take into account the lateral dynamic stresses generated during axially impact. The changes of the cohesion (c) and the friction angle (ϕ) with increasing strain rate reveal the deformation localization properties of concrete-like materials. At higher strain rate loading, larger velocity gradient ($\partial V/\partial x$, here, x denotes the impact direction) generates in the specimen according to the continuity condition: $\partial V/\partial x = \partial \varepsilon/\partial t$, the granites are failed due to local shear failure when local gradient is large enough (Zhou et al., 2018).

Mogi (1967, 1971) had conducted series of experiments of rocks under quasi-static triaxial compression to analyze the static strength of rocks. According to Mogi approach, the present experimental data of dynamic strength are plotted in the σ_1-σ_2 plane, which illustrated in Fig. 13. The data are distributed between the line $\sigma_1 = \sigma_2$ and the curve $\sigma_2 = \sigma_3$. These dashed curves denote the fitting D-P criterion by employing the material parameters (α_0 and k_0) calculated based on the stress state described by Eq. (15), and it shows good consistence with the experimental data at the initial stage. Similar to the static triaxial compression, the D-P model could be well used in the vicinity of the

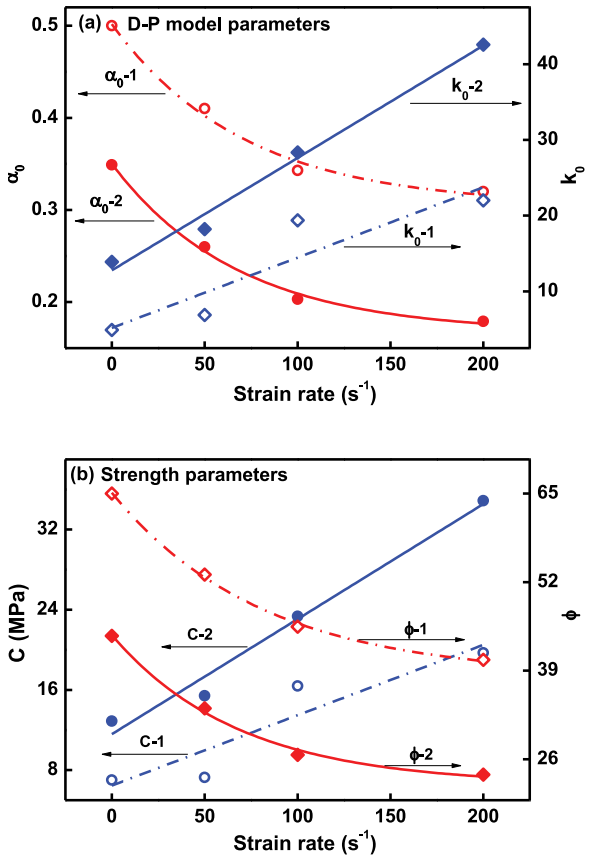

Fig. 12. The D-P criterion parameters (a) and the strength parameters (b) at various strain rates. In the figure, α_0-1 denotes α_0 calculated by the stress state described by Eq. (14), and α_0-2 denotes α_0 calculated by the stress state described by Eq. (15).

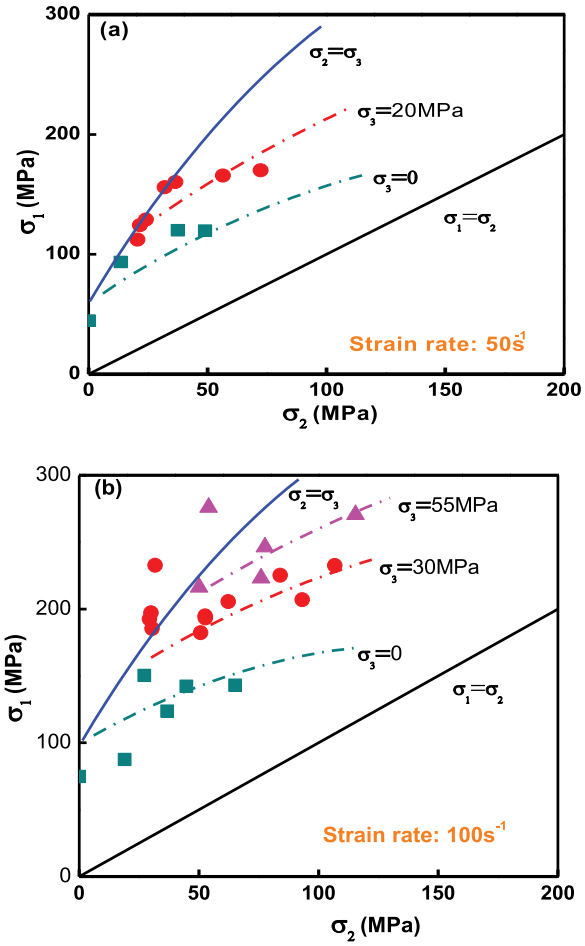

Fig. 13. The strength statistics in σ_1-σ_2 plane at strain rates 50 s^{-1} (a) and 100 s^{-1} (b) the under various σ_3 confinement.

intermediate and minor principal stresses, from which the parameters of the model are obtained. Since the effects of the intermediate and the minor principal stresses are identical in the model, the differences between the predictions and the experimental results increase with increasing the value of (σ_2-σ_3).

6. Conclusions and remarks

A new technique is established to investigate the dynamic behaviors of concrete materials under static triaxial confinements. The advantage of the technique is to apply the triaxial confinements on the specimen and to measure the dynamic triaxial responses of the specimen by six lateral bars. It provides a more powerful method to simulate in-situ dynamic loading process of concrete-like materials under complex stress state. Since the effect of tractions between the specimen and the lateral bar on the impact process is negligible, a valid data processing method is proposed respectively along three directions based on the measured waves, i.e. ε_i, ε_r, and ε_t in the x-axis, $\varepsilon_{y\text{-}left}$ and $\varepsilon_{y\text{-}right}$ in the y-axis, and $\varepsilon_{z\text{-}up}$ and $\varepsilon_{z\text{-}down}$ in the z-axis. Series experiments of a concrete at various strain rates and under various triaxial confinements are conducted.

As presented in Appendix B, the effect of lateral inertia on the uniaxial strength is evaluated partially by the measured wave profiles in the lateral bars when the lateral confinements are zero. The preliminary results show that when taking into account the lateral inertia, the dynamic strength is 6% lower at strain rate 50 s^{-1} and 14.5% lower at strain rate 100 s^{-1}.

The relationships of dynamic stress and strain, the volume strain and the hydrostatic pressure, and the equivalent strain and stress exhibit obvious strain rate effect and load-path dependency. When employing the D-P criterion to describe the dynamic strength, both material parameters (α_0 and k_0) and strength parameters (c and ϕ) show obvious strain rate effect. The results show that with the increasing of strain rate, the friction angle (ϕ) increases, and the cohesion (c) decreases. The effects of the intermediate stress on the strength could be fully investigated by the present technique.

The present 3-D SHPB technique is an improvement over the traditional steel ring confinement technique and the oil-vessel confinement technique. The initial confining pressures can be independently applied in the X, Y and Z directions, and the pressure changes can be independently measured during the x-axis impacting. It merits attention that the present experimental system is somewhat complicated, and the steel ring confinement technique should be a powerful and efficient supplement for simpler loading conditions.

Acknowledgements

The experiments are carried out on the 3-D compressed and monitored Hopkinson bar of Monash University, Australia. Many thanks should be given to Prof Jian Zhao of Monash University for his extraordinary vision on the experimental apparatus, and Dr Qianbin Zhang of Monash University is appreciated for his wonderful suggestions. This work is partially supported by the National Natural Science Foundation of China (Grant Nos: 11672286, 11602267, 11472264) and CNPC-CAS Strategic cooperation Research Program (Grant No: 2015A-4812).

Appendix A. Data processing method considering the lateral tractions

A1: Data processing method

As shown in Fig. A1(a), the true triaxial stress state ($\sigma_{x\text{-static}} \neq \sigma_{y\text{-static}} \neq \sigma_{z\text{-static}}$) is firstly applied on the cubic specimen by six bars. Seven wave profiles, e.g. the elastic incident wave (ε_i), the reflected wave (ε_r), the transmission wave (ε_t), and four lateral waves (e.g. $\varepsilon_{y\text{-}left}$, $\varepsilon_{y\text{-}right}$, $\varepsilon_{z\text{-}up}$, and $\varepsilon_{z\text{-}down}$), are generated during the x-axis impacting. The tractions between the specimen and the lateral bar are then generated due to specimen compression in the impact direction, e.g. $\tau_{yx\text{-}left}$ and $\tau_{yx\text{-}right}$ on the opposite surfaces in the y-axis, $\tau_{zx\text{-}up}$ and $\tau_{zx\text{-}down}$ on the opposite surfaces in the z-axis. If the force equilibrium assumption is satisfied along the impact direction, the equation could be obtained as follows.

The force on the input surface is:

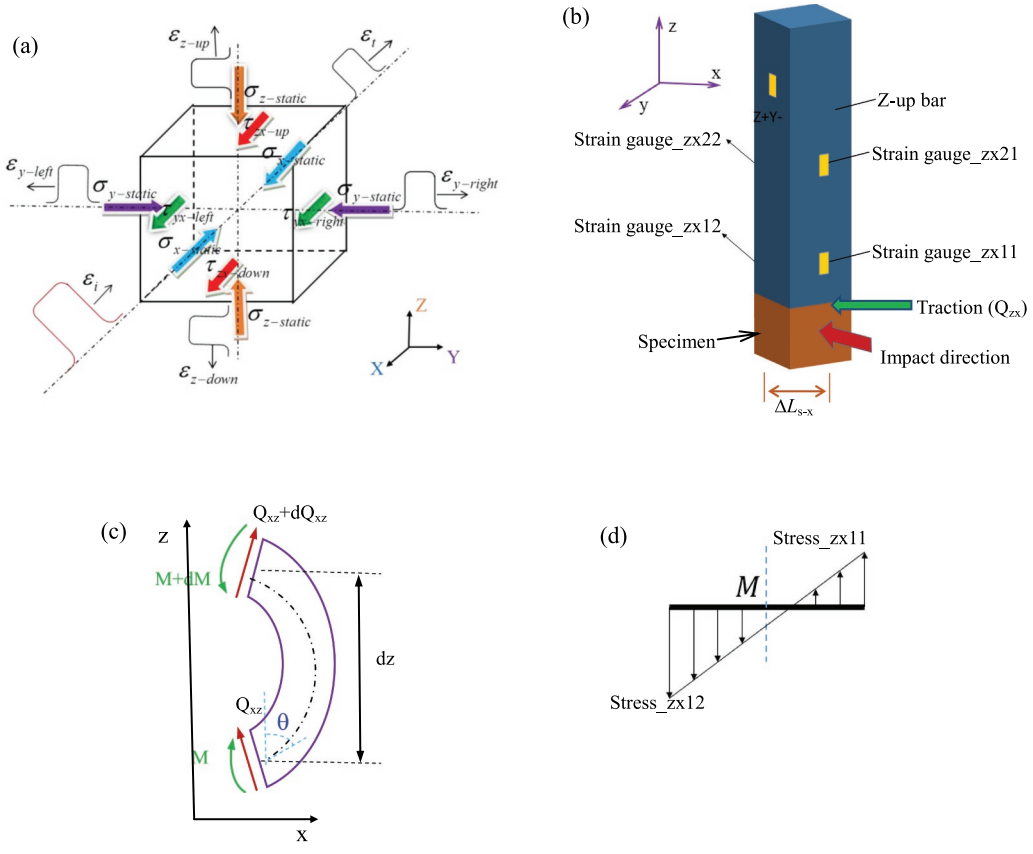

Fig. A1. Schematic diagrams of lateral shear stress measurement: (a) the static confinement and dynamic stresses (including normal stresses and shear stresses) applied on the specimen, (b) force analyses of the z-up bar, (c) the traction and the moment applied on the microelement, (d) stress distribution across the specimen section.

$$F_I = (\sigma_i + \sigma_r)A_0 = E_0(\varepsilon_i + \varepsilon_r)A_0 \tag{A1}$$

The force on the output surface is:

$$F_{II} = \sigma_t A_0 = E_0 \varepsilon_t A_0 \tag{A2}$$

The force on the lateral surfaces is:

$$F_{ILateral} = (\tau_{yx-left} + \tau_{yx-right})A_{s-y} + (\tau_{zx-up} + \tau_{zx-down})A_{s-z} \tag{A3}$$

And then, the force equilibrium assumption requires that $F_I \approx F_{II} + F_{Lateral}$. Therefore, in the x-axis, the stress applied on the specimen could be expressed as:

$$\sigma_{s-x} = \frac{1}{2A_{s-x}}[E_0(\varepsilon_i + \varepsilon_r)A_0 + E_0\varepsilon_t A_0 + (\tau_{yx-left} + \tau_{yx-right})A_{s-y} + (\tau_{zx-up} + \tau_{zx-down})A_{s-z}] \tag{A4}$$

For a cubic specimen, it could be simplified to be

$$\sigma_{s-x} = \frac{E_0}{2}\left[(\varepsilon_i + \varepsilon_r + \varepsilon_t)\frac{A_0}{A_{s-x}} + \frac{1}{E_0}(\tau_{yx-left} + \tau_{yx-right} + \tau_{zx-up} + \tau_{zx-down})\right] \tag{A5}$$

The strain rate ($\dot{\varepsilon}_{x-dyn}$) and the strain ($\varepsilon_{x-dyn}$) could be determined respectively by Eqs. (1) and (2). In the y-axis and the z-axis, the strain (ε_{k-dyn}) and the dynamic stress (σ_{k-dyn}) could be determined respectively by Eqs. (5) and (6). Among then, these four tractions between the specimen and the lateral bar should be measured simultaneously.

A2: measurement and calculation of the traction

As shown in Fig. A1(b), analysis of the traction between the specimen and the z-up bar is chosen as an example. When the traction (Q_{zx}) is applied on the bar end, a flexural wave propagates along the bar, and the traction could be determined by measuring the flexural wave. Two pairs of strain gauges (i.e. zx11 and zx12, zx21 and zx22) are stuck on the z-up bar to measure the velocity of the flexural wave, and the gauges stuck to the opposite sides (i.e. zx11 and zx12) are used to measure the compression signal and the tensile signal of one section along the z-up bar (Fig. A1(d)).

As illustrated in Fig. A1(c), the traction (Q_{zx}) is expressed as:

$$Q_{zx} = \frac{dM}{dz} + \rho_0 I \frac{d\omega}{dt} \tag{A6}$$

where, M is the section moment, I is the moment of inertia of the z-axis, and ω is the angular velocity of section rotation.

As illustrated in Fig. A1(d), at the section of gauges zx11 and zx12 stuck on, the measured signals of ε_{zx11} and ε_{zx12} consist of the compression signal and the flexural wave signal, and they are expressed as: $\varepsilon_{zx11} = \varepsilon^1_{flex} + \varepsilon_{comp}$, and $\varepsilon_{zx12} = \varepsilon^2_{flex} + \varepsilon_{comp}$. Where, ε_{comp} denotes the compression strain along the z-up bar. ε^1_{flex} and ε^2_{flex} are respectively the signals of the flexural wave at positions zx11 and zx12, and they satisfy: $\varepsilon^1_{flex} = -\varepsilon^2_{flex}$. Then, the compression signal and the flexural signal should be distinguished from these two signals, and listed as:

$$\varepsilon_{comp} = (\varepsilon_{zx11} + \varepsilon_{zx12})/2 \tag{A7}$$

$$\varepsilon^1_{flex} = -\varepsilon^2_{flex} = \varepsilon_{zx11} - \varepsilon_{comp} \tag{A8}$$

Let ε_{flex}=$|\varepsilon^1_{flex}| = |\varepsilon^2_{flex}|$, the section moment M can be expressed as:

$$M = \frac{E_0 L^3_{s-z}}{6} \varepsilon_{flex} \tag{A9}$$

And then, it obtains that

$$\frac{dM}{dz} = \frac{dM}{dt}\frac{dt}{dz} = \frac{E_0 L^3_{s-z}}{6c_f}\frac{d\varepsilon_{flex}}{dt} \tag{A10}$$

where, c_f is the velocity of the flexural wave, and $c_f \equiv dz/dt$. Here, the flexural wave is described by $z = z\ (t)$.

The angular velocity $\omega = \frac{d\theta}{dt}$, and $d\theta$ satisfies: $d\theta = \frac{M}{E_0 I} ds = \frac{M}{E_0 I}(1 + \varepsilon_{flex}) dz$. Here, ds is the arch length. And then, we obtain:

$$\omega = \frac{d\theta}{dt} = \frac{M}{E_0 I}(1 + \varepsilon_{flex}) c_f \tag{A11}$$

The second term on the right side of Eq. (A6) is rewritten as

$$\rho_0 I \frac{d\omega}{dt} = \rho_0 I \frac{c_f}{E_0 I}\left[\frac{dM}{dt}(1 + \varepsilon_{flex}) + M\frac{d\varepsilon_{flex}}{dt}\right] = \frac{E_0 L^3_{s-z}}{6c_f}(1 + 2\varepsilon_{flex})\frac{d\varepsilon_{flex}}{dt} \tag{A12}$$

Therefore, Eq. (A6) could be rewritten as follows.

$$Q_{zx} = \frac{E_0 L^3_{s-z}}{3c_f}(1 + \varepsilon_{flex})\frac{d\varepsilon_{flex}}{dt} \tag{A13}$$

$$\tau_{zx-up} = \frac{Q_{zx}}{A_{s-z}} = \frac{E_0 L_{s-z}}{3c_f}(1 + \varepsilon_{flex})\frac{d\varepsilon_{flex}}{dt} \tag{A14}$$

The traction at the positions zx21 and zx22 can be calculated accordingly.

A3: Results

A steel cubic specimen is firstly used to validate the data processing method. For the conventional SHPB device, there would be no reflected wave in the impact bar when the specimen and the bars are both made of steel. In the present 3-D bars system and as shown in Fig. A2(a), the reflected wave (ε_r) with lower amplitude and with shorter duration is observed. By the three-wave (ε_i, ε_r, and ε_t) method, the stress equilibrium along the x-axis is achieved, as illustrated in the middle of Fig. A2(a). The reflected wave generates during the lateral expanding of the steel specimen, and its amplitude seems to decrease slightly with increasing the lateral confinement, which demonstrated at the middle top in Fig. A2(a).

Fig. A2(b) illustrates the recorded wave profiles in the z-up bar. The first pair of gauges (i.e. zx11 and zx12 as shown in Fig. A1(b)) are bonded 50 mm apart from the bar end. The calculated compression signal (ε_{comp}, 'z-comp' in Fig. A2(b)) is consistent well with the measured compressional signal ($\varepsilon_{z\text{-}up}$). The velocity of the flexural wave, c_f, is determined by the distance and the time interval of two pairs of gauges and calculated to be 2400 m/s. And then, the shear stresses between the specimen and the lateral bar are calculated by Eq. (A14). There are some differences between the results calculated on strain signals at zx11 and those at zx21 due to wave dispersion, and only the results at zx11 are presented in the present study.

Fig. A2(c) and (d) demonstrate the shear stresses on the lateral surface during the x-axis impacting. The results show that when the impact velocity is 12 m/s, the amplitude of shear stresses increases with increasing the lateral confinements, e.g. 1.72 MPa and 1.80 MPa under confinement 8 MPa, 2.66 MPa under confinement 16 MPa, 2.91 MPa under confinement 20 MPa, 2.84 MPa under confinement 40 MPa, and 3.01 MPa under confinement 60 MPa. Durations of the shear stress are much shorter than that of the incident wave (ε_i). Once the incident pulse applied along the x-direction, the sample is compressed and the lateral shear stresses are stimulated. With increasing compressional deformation of the sample, the lateral shear stresses increase firstly, and then decrease quickly when the interface of sample and bar starts to slide. The results indicate that the shear stresses applied on the lateral surface of specimen is transient and at local. The corresponding area that the maximum shear stress applied is much lower than the area of lateral surface, and the lateral shear stresses have less effect on the overall stress equilibrium. Since the shear stresses are

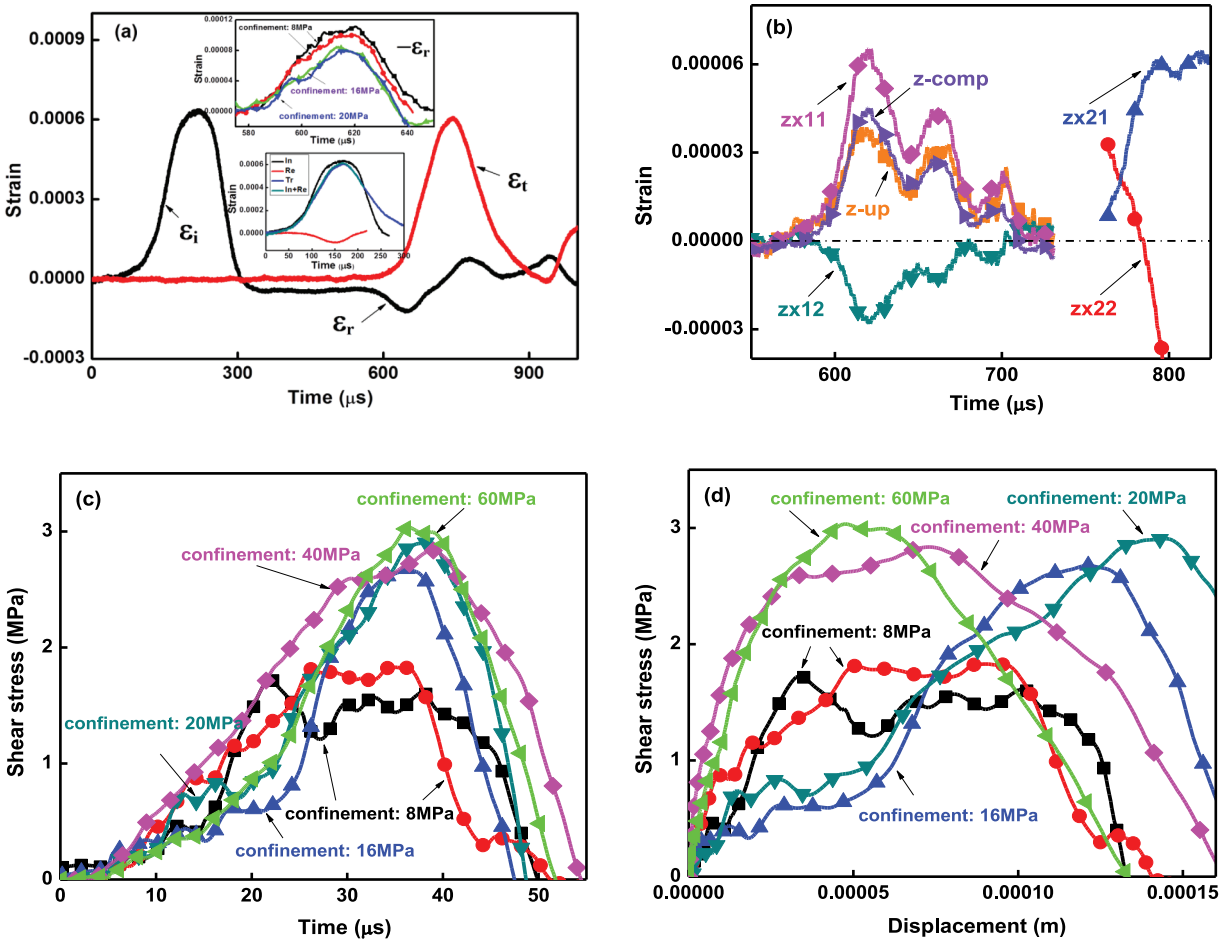

Fig. A2. Wave profiles of the flexural wave and lateral traction property (steel, impact velocity 12 m/s): wave profiles in the x-axis (b) the flexural wave profiles in the z-up bar, (c) the calculated lateral shear stress profiles, (d) relationship of lateral shear stress to specimen compressional displacement.

generated due to the axially compression of specimen, relationship of the shear stresses and the compression displacement of specimen ($\Delta L_{s\text{-}x}$) is formed and illustrated in Fig. A2(d). The curves show evident the peak value of shear stress, and there is stress-drop after the peak. Under confinement 8 MPa, the shear stresses reach the peak value at compression displacement 0.04–0.05 mm and long distance dynamic surface sliding occurs after the peak, and under confinements 16 MPa and 20 MPa, the shear stresses reach its peak at displacement 0.12–0.14 mm. The compressional displacements should be approximately used to evaluate the critical displacement of surface sliding.

These results of concrete specimen are demonstrated in Fig. A3. Fig. A3(a) illustrates the recorded typical waveforms in the x-axis. Compared with the steel specimen, amplitude of the reflected wave (ε_i) is much higher due to impedance mismatch of steel bar and the concrete specimen. By the three-wave (ε_i, ε_r, and ε_t) method and as demonstrated at the middle top in Fig. A3(a), the stress equilibrium along the x-axis is achieved. Fig. A3(b) illustrates the recorded wave profiles in the z-up bar. The calculated compressional signal (ε_{comp}, 'z-comp' in Fig. A3(b)) is consistent well with the measured compressional signal ($\varepsilon_{z\text{-}up}$). The velocity of the flexural wave is about 2400 m/s. The shear stresses between the specimen and the lateral bar could be calculated by Eq. (A14).

Fig. A3(c) and (d) demonstrate the shear stresses on the lateral surface when the x-axially impacting velocity is 10 m/s. The results show that the amplitude of shear stresses is scattered distributed with increasing the lateral confinements, e.g. 3.10 MPa under confinement 8 MPa, 3.44 MPa under confinement 12 MPa, 2.44 MPa under confinement 16 MPa, 3.38 MPa under confinement 20 MPa, 3.50 MPa under confinement 40 MPa, and 3.60 MPa under confinement 60 MPa. Durations of the shear stress are much shorter than that of the incident wave (ε_i), which lead to the corresponding area that the maximum shear stress applied much lower than the area of lateral surface. Therefore, the lateral shear stresses have less effect on the overall stress equilibrium. The curves in Fig. A3(d) show evident the peak value of shear stress and long distance dynamic surface sliding occurs after the peak. Under six confinements, i.e. 8, 12, 16, 20, 40, and 60 MPa, the shear stresses reach the peak value at compressional displacement 0.12, 0.16, 0.08, 0.06, 0.05, and 0.02 mm, respectively. The compressional displacements should be approximately used to evaluate the critical displacement of surface sliding. These results show also the complexity of concrete surface.

The shear stresses applied on the lateral surface of specimen is transient and at local. Therefore, the corresponding area that the maximum shear stress applied is much lower than the area of lateral surface, and the lateral shear stresses could have less effect on the overall stress equilibrium. It could be ignored in the calculation of the strain rate ($\dot{\varepsilon}_{x-dyn}$), the strain ($\varepsilon_{x-dyn}$), and the dynamic stress (σ_{x-dyn}) in the x-axis. In addition, the technique provides a useful tool to measure the dynamic friction of interfaces.

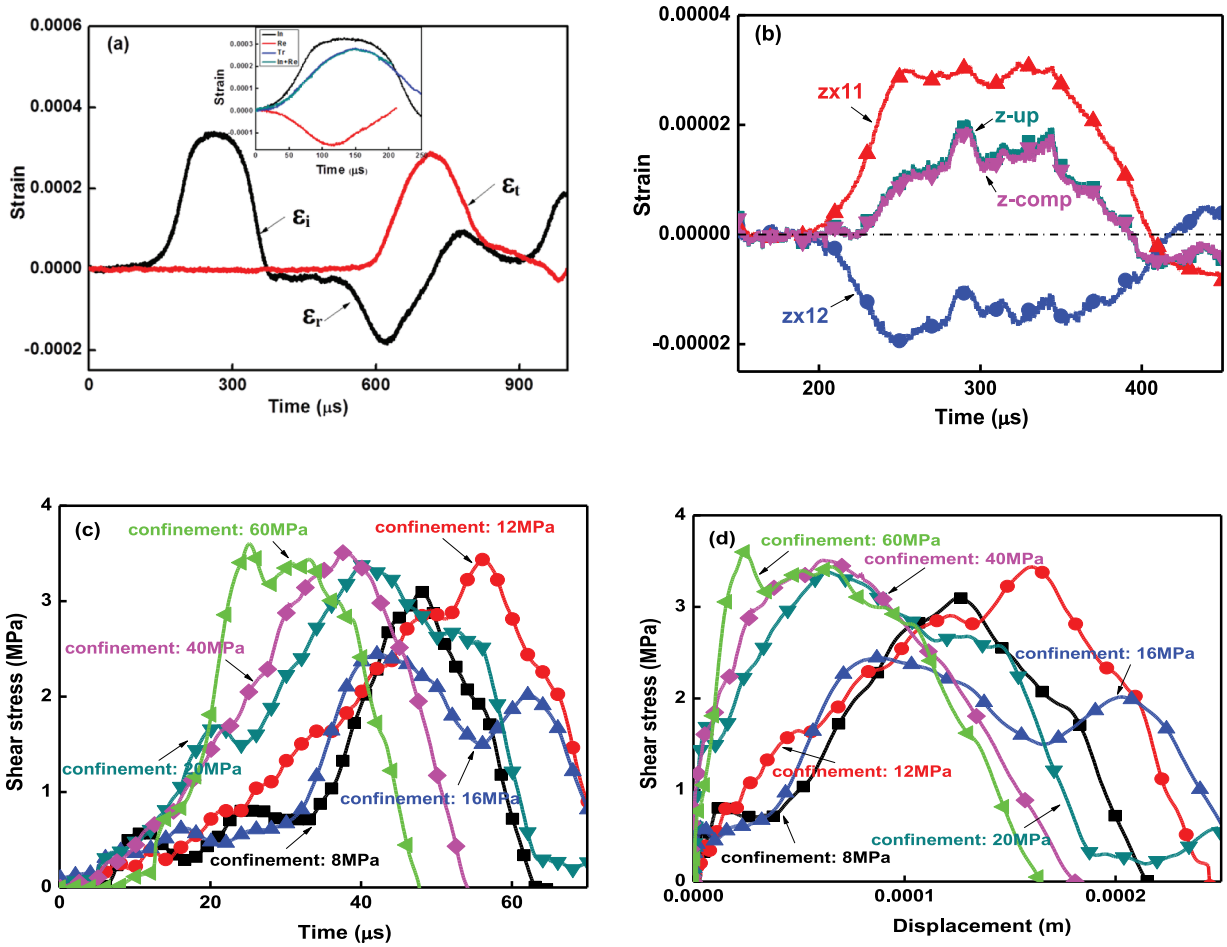

Fig. A3. Wave profiles of the flexural wave and lateral traction property (concrete, impact velocity 10 m/s): (a) wave profiles in the x-axis, (b) the flexural wave profiles in the z-up bar, (c) the calculated lateral shear stress profiles, (d) relationship of lateral shear stress to specimen compressional displacement.

Appendix B. The radial inertia effect

Dynamic strengths of the concrete-like materials are sensitive to the hydrostatic stress due to the local lateral inertia confinement (Li and Meng, 2003; Meng and Li, 2003a,b). Grote et al. (2001) had evaluated respectively the effects of the rate-dependence and the hydrostatic pressure dependence by comparing the experimental results of SHPB to those of the plate impact. The radial inertia effect is generated due to the distributed radial stress when the specimen subjected to axially impacting. The radial stress σ_r of compressible samples had been deduced by Forrestal et al. (2007) and could be expressed as: $\sigma_r = \frac{\nu(3-2\nu)}{8(1-\nu)}\rho_0\ddot{\varepsilon}_x(r^2 - a_0^2)$, where, r and a_0 were the cylindrical coordinate and radius of the sample, ρ_0 and ν were respectively the density and poison's ratio of the samples, and $\ddot{\varepsilon}_x$ was strain acceleration along the impact direction. The result provided distributed lateral confinement for an axially impacted sample.

The radial stress of the specimen under hydrostatic confinement could be derived based on Forrestal et al. (2007) method and replace the

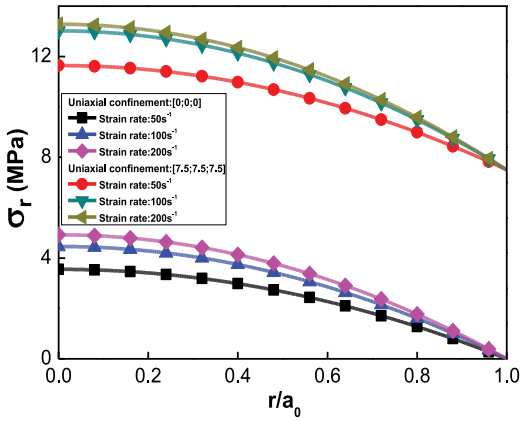

Fig. B1. Distribution of radial stress.

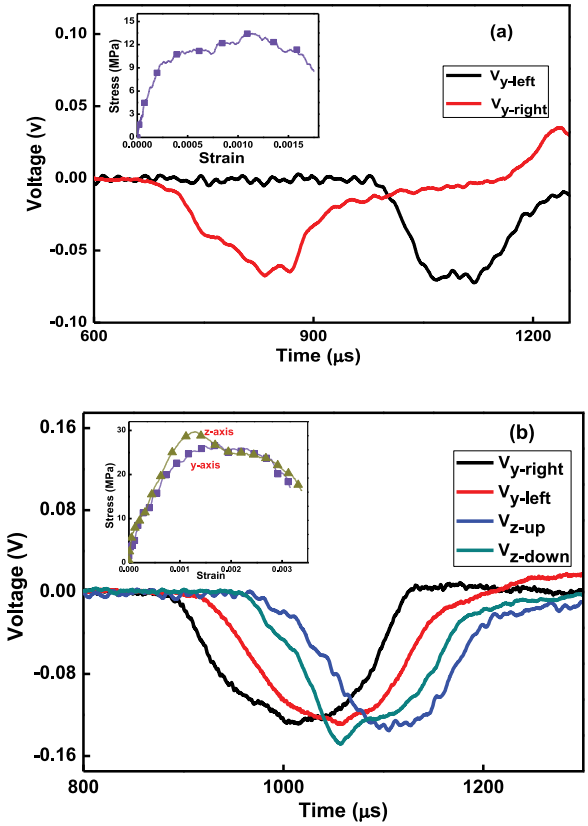

Fig. B2. Recorded waveforms in the bars with lateral confinement zero. (a) The y-axis disturbance for biaxial confinement, (b) The disturbances in the y-axis and the z-axis for triaxial confinement.

constraint condition as: $u^1(r=0)=0$, and $\sigma_r(r=a_0)=-p$. Where, p is the hydrostatic pressure applied on the specimens. The radial displacement u^1 and radial stress σ_r can be obtained as:

$$u^1=\frac{\nu(1+\nu)(1-2\nu)}{8(1-\nu)E}r\left[\rho_0\ddot{\varepsilon}_x(r^2-(3-2\nu)a_0^2)+p\frac{8(1-\nu)}{\nu}\right] \tag{B1}$$

$$\sigma_r=\frac{\nu(3-2\nu)}{8(1-\nu)}\rho_0\ddot{\varepsilon}_x(r^2-a_0^2)+p \tag{B2}$$

Eq. (B2) is used to roughly evaluate the radial inertia effect. Fig. B1 demonstrates the calculated radial stresses under various confinements and various strain rates based on the experimental strain rate profiles. The radial stresses increase with increasing confining pressure and/or strain rate. Forquin et al. (2008) had used the mental ring to reduce the radial displacement, which could illustrated by Eq. (B1), and confine the lateral inertia of the concrete specimen. Zhang et al. (2009, 2010) had used tubular specimen to reduce the radial inertia, which could illustrated by Eq. (B2) with smaller r and a_0 for tubular structure. These special treatments had dealt well with the effect of radial inertia on the dynamic strength.

In the present study, the effects of lateral inertia could be evaluated partially by the measured wave profiles in the lateral bars. When the specimen is impacted axially, the local lateral inertia is generated, and its effects might propagate to the lateral surfaces of the specimen. To provide comparison with the conventional SHPB tests, specimen under lateral confinement zero is chosen for further discussions.

Fig. B2(a) demonstrates the recorded waveforms in the right bar and the left bar of the y-axis with lateral confinement zero. When the impact velocity is 13.3 m/s, the x-axis strain rate is about 50 s^{-1}, and the dynamic stress in the y-axis reaches to 13.3 MPa. It consists of mainly two effects, i.e. the Poisson effect and the lateral tractions. Some additional experimental results demonstrated in Appendix A give much lower values of the lateral tractions. Therefore, the dynamic stress in the y-axis is generated mainly by the Poisson effect which induced by the radial inertia. Employing the effective strength σ_e ($\sigma_e=\sqrt{(\sigma_x-\sigma_y)^2+(\sigma_y-\sigma_z)^2+(\sigma_z-\sigma_x)^2}/\sqrt{2}$) to describe the strength properties, the dynamic strength is calculated to be 87.55 MPa, and 6% lower than σ_x (93.5 MPa).

Fig. B2(b) demonstrates the recorded waveforms in four lateral bars with lateral confinements zero. When the impact velocity is 20.8 m/s, the x-axis strain rate is 100 s^{-1}, and the dynamic stresses in the y-axis and the z-axis reach respectively to 26.5 MPa and 29.4 MPa. The dynamic effective strength is calculated to be 164.59 MPa, and 14.5% lower than σ_x (192.5 MPa).

These two results illustrate preliminarily the effects of radial inertia on the dynamic strength, which much lower than the effects, e.g. 52%, in the plate impact experiments reported by Grote et al. (2001). Further efforts should be made to distinguish the ratio of radial inertia effect on the dynamic strength by the present technique.

References

Alejano, L., Bobet, A., 2012. Drucker- Prager criterion. Rock Mech. Rock Eng. 45, 995–999.

Bailly, P., Delvare, F., Vial, J., Hanus, J., Biessy, M., Picart, D., 2011. Dynamic behavior of an aggregate material at simultaneous high pressure and strain rate: SHPB triaxial tests. Int. J. Impact Eng. 38 (2), 73–84.

Bažant, Z.P., Kim, S., 1979. Plastic-fracturing theory for concrete. J. Eng. Mech. ASCE 105 (3), 407–428.

Bažant, Z.P., Bishop, F., Chang, T., 1986. Confined compression tests of cement paste and concrete up to 300 ksi. ACI J. 83, 553–560.

Bažant, Z.P., Oh, B.H., 1985. Microplane model for progressive fracture of concrete and rock. J. Eng. Mech. ASCE 111 (4), 559–582.

Burlion, N., Gatuingt, F., Pijaudier-Cabot, G., Daudeville, L., 2000. Compaction and tensile damage in concrete: constitutive modeling and application to dynamics. Comput. Methods Appl. Mech. Eng. 183, 291–308.

Cadoni, E., 2013. Mechanical characterization of rock materials at high strain-rate. In: Jian, Zhao, Jianchun, Li (Eds.), Rock Dynamics and Applications-States of Art. CRC Press, Hoboken, pp. 137–148.

Cadoni, E., Albertini, C., 2011. Modified hopkinson bar technologies applied to the high strain rate rock tests. In: Zhou, YX, Zhao, J (Eds.), Advances in Rock Dynamics and Application. CRC Press, Hoboken, pp. 79–104.

Cadoni, E., Dotta, M., Forni, D., Riganti, G., Albertini, C., 2015. First application of the 3D-MHB on dynamic compressive behavior of UHPC. In: EPJ Web of Conferences. 94. pp. 01031.

Chen, W., Ravichandran, G., 1996. An experimental technique for imposing dynamic multi-axial compression with mechanical confinement. Exp. Mech. 36, 155–158.

Chen, W., Ravichandran, G., 1997. Dynamic compressive failure of a glass ceramic under lateral confinement. J. Mech. Phys. Solids 45, 1303–1328.

Chen, W., Song, B., 2011. Split Hopkinson (Kolsky) bar: design. Testing and Applications. Springer, New York.

Christensen, R.J., Swanson, S.R., Brown, W.S., 1972. Split Hopkinson bar test on rock under confining pressure. Exp. Mech. 12, 508–541.

Cui, J., Hao, H., ASCE, F., et al., 2019. Volumetric properties of concrete under true triaxial dynamic compressive loadings. J. Mater. Civil. Eng. 31 (7), 04019126.

Drucker, D., Prager, W., 1952. Soil mechanics and plastic analysis for limit design. Q. Appl. Math. 10 (2), 157–165.

Forquin, P., Arias, A., Zaera, R., 2007. An experimental method of measuring the confined compression strength of geomaterials. Int. J. Solids Struct. 44, 4291–4317.

Forquin, P., Gary, G., Gatuingt, F., 2008. A testing technique for concrete under confinement at high rates of strain. Int. J. Impact Eng. 35, 425–446.

Forquin, P., Safa, K., Gary, G., 2010. Influence of free water on the quasi-static and dynamic strength of concrete in confined compression tests. Cement Concrete Res. 40 (2), 321–333.

Forrestal, M.J., Wright, T.W., Chen, W., 2007. The effect of radial inertia on brittle samples during the split Hopkinson pressure bar test. Int. J. Impact Eng. 34, 405–411.

Frew, D., Akers, S., Chen, W., Green, M., 2010. Development of a dynamic triaxial Kolsky bar. Meas. Sci. Technol. 21, 105704.

Frew, D., Forrestal, M., Chen, W., 2002. Pulse shaping techniques for testing brittle materials with a split Hopkinson pressure bar. Exp. Mech. 42, 93–106.

Gary, G., Bailly, P., 1998. Behavior of a quasi-brittle material at high strain rate. Exp. Model. Eur. J. Mech. 17 (3), 403–420.

Gerstle, K.H., 1980. Behavior of concrete under multiaxial stress states. J. Eng. Mech. ASCE 106 (6), 1383–1403.

Gran, J.K., Florence, A.L., Colton, J.D., 1989. Dynamic triaxial tests of high-strength concrete. J. Eng. Mech. 115 (5), 891–904.

Grote, D.L., Park, S.W., Zhou, M., 2001. Dynamic behavior of concrete at high strain rates and pressures: I. experimental characterization. Int. J. Impact Eng. 25, 869–886.

Handin, J., Heard, H.C., Magouirk, J.N., 1967. Effect of the intermediate principal stress on the failure of limestone, dolomite, and glass at different temperatures and strain rates. J. Geophy. Res. 72, 611–640.

Hoek, E., Brown, E.T., 1997. Practical estimates of rock mass strength. Int. J. Rock Mech. Min. Sci. 34, 1165–1186.

Horii, H., Nemat-Nasser, S., 1986. Brittle failure in compression: splitting, faulting and brittle-ductile transition. Phil. Trans. Royal. Soc. Lond. A319, 337–374.

Huang, J., E, J., Huang, J., et al., 2016b. Dynamic deformation and fracture of single crystal silicon: fracture modes, damage laws, and anisotropy. Acta Mater. 114, 136–145.

Huang, J., Lu, L., Fan, D., et al., 2016a. Heterogeneity in deformation of granular ceramics under dynamic loading. Scripta Mater. 111, 114–118.

Huang, J., Xu, S., Hu, S., 2013. Effects of grain size and gradation on the dynamic responses of quartz sands. Int. J. Impact Eng. 59, 1–10.

Huang, J., Xu, S., Hu, S., 2014. Influence of particle breakage on the dynamic compression responses of brittle granular materials. Mech. Mater. 68, 15–28.

Hummeltenberg, A., Curbach, M., 2012. Design and construction of a biaxial split-Hopkinson-bar. Beton-Und Stahlbetonbau 107 (6), 394–400.

Li, H.B., Zhao, J., Li, T.J., 1999. Triaxial compression tests of a granite at different strain rates and confining pressures. Int. J. Rock Mech. Min. Sci. 36, 1057–1063.

Li, Q.M., Meng, H., 2003. About the dynamic strength enhancement of cement-like materials in a split Hopkinson pressure bar test. Int. J. Solids Struct. 40 (2), 343–360.

Liu, K., Zhang, Q., Wu, G., et al., 2019. Dynamic mechanical and fracture behaviour of sandstone under multiaxial loads using a triaxial Hopkinson bar. Rock Mech. Rock Eng. 1–21.

Lubarda, V., Mastilovic, S., Knap, J., 1996. Brittle-ductile transition in porous rocks be cap model. J. Eng. Mech. 122 (7), 633–642.

Malvern, L.E., Ross, C.A., 1985. Dynamic response of concrete and concrete structures. Second Annual Technical Report, AFOSR contract no. F49620-83-K007.

Meng, H., Li, Q.M., 2003a. Correlation between the accuracy of a SHPB test and stress uniformity based on numerical experiments. Int. J. Impact Eng. 28 (5), 537–555.

Meng, H., Li, Q.M., 2003b. Modification of SHPB set-up to minimize wave dispersion and attenuation effects. Int. J. Impact Eng. 28 (6), 677–696.

Mogi, K., 1967. Effect of the intermediate principal stress on rock failure. J. Geophys. Res. 72, 5117–5131.

Mogi, K., 1971. Fracture and flow of rocks under high triaxial compression. J. Geophys. Res. 76, 1255–1269.

Nemat-Nasser, S., Choi, J.Y., Guo, W.G., Isaacs, J.B., 2005. Very high strain- rate response of a NiTi shape-memory alloy. Mech. Mater. 37 (2), 287–298.

Piotrowska, E., Forquin, P., Malecot, Y., 2016. Experimental study of static and dynamic behavior of concrete under high confinement: effect of coarse aggregate strength. Mech. Mater. 92, 164–174.

Piotrowska, E., Malecot, Y., Ke, Y., 2014. Experimental investigation of the effect of coarse aggregate shape and composition on concrete triaxial behavior. Mech. Mater. 79, 45–57.

Ross, C.A., Jerome, D.M., Tedesco, J.W., Hughes, M.L., 1996. Moisture and strain rate effects on concrete strength. ACI Mater. J. 93 (3), 293–300.

Ross, C.A., Tedesco, J.W., Kuennen, S.T., 1995. Effects of strain rate on concrete strength. ACI Mater. J. 92 (1), 37–47.

Ross, C.A., Thomson, P.Y., Tedesco, J.W., 1989. Split-Hopkinson pressure-bar test on concrete and mortar in tension and compression. ACI Mater. J. 86 (5), 475–481.

Song, B., Chen, W., Luk, V., 2009. Impact compressive response of dry sand. Mech. Mater. 41 (6), 777–785.

Tang, Z., Xu, S., Dai, X., et al., 2005. S-wave tracing technique to investigate the damage and failure behavior of brittle materials subjected to shock loading. Int. J. Impact Eng. 31, 1172–1191.

Tedesco, J.W., Ross, C.A., 1998. Strain-rate-dependent constitutive equations for concrete. ASME J. Press. Vessel Technol. 120, 398–405.

Xu, S., Huang, J., Wang, P., et al., 2015. Investigation of rock material under combined compression and shear dynamic loading: an experimental technique. Int. J. Impact Eng. 86, 206–222.

Xu, S., Wang, P., Shan, J., Zhang, M., Zhou, L., 2018. Dynamic behavior of concrete under static tri-axial loadings. J. Vib. Shock 37 (15), 59–67 In Chinese.

Xu, S., Wang, P., Zhao, J., Hu, S., 2017. Dynamic behaviors of concrete under static triaxial loading using “3D-Hopkinson bar”. Explos. Shock Waves 37 (2), 180–185 In Chinese.

Xu, S., Zhao, J., Song, X., et al., 2016. A Modified SHPB Device for Rock Specimen Under True-Triaxial Static Confinement. China patent, CN201620574575.9, 2016-6-15 (In Chinese).

Zhang, M., Li, Q.M., Huang, F.L., Wu, H.J., Lu, Y.B., 2010. Inertia-induced radial confinement in an elastic tubular specimen subjected to axial strain acceleration. Int. J. Impact Eng. 37 (4), 459–464.

Zhang, M., Wu, H.J., Li, Q.M., Huang, F.L., 2009. Further investigation on the dynamic compressive strength enhancement of concrete-like materials based on split Hopkinson pressure bar tests part I: experiments. Int. J. Impact Eng. 36 (12), 1327–1334.

Zhang, Q.B., Zhao, J., 2014. A review of dynamic experimental techniques and mechanical behavior of rock material. Rock Mech. Rock Eng. 47 (4), 1411–1478.

Zhao, J., 2000. Applicability of Mohr-Coulomb and Hoek-Brown strength criteria to the dynamic strength of brittle rock. Int. J. Rock Mech. Min. Sci. 37 (3), 1115–1121.

Zhao, J., Wu, W., Zhang, Q., et al., 2013. Some recent developments on rock dynamic experiments and modeling. In: Jian, Zhao, Jianchun, Li (Eds.), Rock Dynamics and Applications-States of Art. CRC Press, Hoboken, pp. 25–40.

Zhou, L., Xu, S., Shan, J., Liu, Y., Wang, P., 2018. Heterogeneity in deformation of granite under dynamic combined compression/shear loading. Mech. Mater. 123, 1–18.